The Glass Ramp of Wrangellia:
Reconstruction of the Late Triassic to Early Jurassic Outer Ramp Environments of the McCarthy Formation, Alaska

Yorick P. Veenma BSc.

Master's thesis

Department of Earth Sciences

Universiteit Utrecht

19 April 2021

First advisor: Dr. João P. Trabucho-Alexandre

Second advisor: Dr. Benjamin C. Gill

Abstract

Following the end-Triassic mass extinction, widespread biogenic ramps on Pangea became glass ramps, which are characterized by siliceous sponge meadows. This transition may represent a global increase in oceanic silica concentrations resulting from the weathering of the Central Atlantic Magmatic Province, but evidence is limited to the continental margins of Pangea. The McCarthy Formation gives us the oceanic perspective, as it represents Norian to Hettangian sedimentation on Wrangellia, an isolated terrane in the Panthalassan Ocean. I therefore analyzed the facies and architecture of the lower and upper member of the McCarthy Formation at Grotto Creek (Wrangell Mountains, Alaska).

The McCarthy Formation records an outer ramp where reworked shallow-water sediment was deposited on lobe complexes. When the supply of reworked sediment was reduced, hemipelagic sedimentation predominated. Bottom currents were active when the upper member was deposited and produced a sediment drift on the outer ramp in the Hettangian. The reworked bioclasts transition across the member boundary from calcareous shell fragments to siliceous spicules, which represents a transition from a siliceous carbonate-ramp to a glass ramp in the Hettangian. This transition coincides with an order of magnitude increase in sedimentation rates, which shows how an increase in shallow-water sediment production increases the sediment supply to the outer ramp. The presence of a glass ramp on Wrangellia supports the hypothesis that a global increase in oceanic silica concentrations promoted widespread biosiliceous sedimentation on ramps.

Acknowledgements

Table of contents

List of figures

List of tables

1. Introduction

Following the end-Triassic mass extinction, biosiliceous sedimentation became more prevalent on ramps, resulting in the rise of glass ramps on Pangea (reviewed in Ritterbush 2019). Glass ramps are biogenic ramps that are characterized by sponge meadows and cherty facies (see also Gates, James, and Beauchamp 2004; Ritterbush 2019). The biogeochemical transition from carbonate ramp to glass ramp is recognized in the Hettangian of Nevada (Ritterbush et al. 2014), Peru (Ritterbush, Ibarra, and Tackett 2016), and Austria (Delecat, Arp, and Reitner 2011). Ritterbush et al. (2015) proposed that this widespread change in the biogeochemical regime of ramps was caused by the weathering of the Central Atlantic Magmatic Province (CAMP) and calculated that CAMP basalts could have supplied enough silica to the oceans to allow sponges to dominate shallow-water ecosystems. However, evidence from ancient ramps is limited to records from the continental margins of Pangea (Ritterbush 2019). The McCarthy Formation, on the other hand, represents Norian to Hettangian sedimentation on Wrangellia – an isolated terrane in the equatorial Panthalassan Ocean (Jones, Silberling, and Hillhouse 1977; Trop et al. 2002) – and therefore represents the oceanic perspective on biosiliceous sedimentation on ramps.

The McCarthy Formation, named after McCarthy Creek by Rohn (1900), is a fine-grained succession that is exposed across the Wrangell Mountains of Alaska (MacKevett 1978). In the last century, the lithologies of the McCarthy Formation were described during explorations (Schrader and Spencer 1901; Moffit and Capps 1911; Martin 1916; Moffit 1930; 1938) and
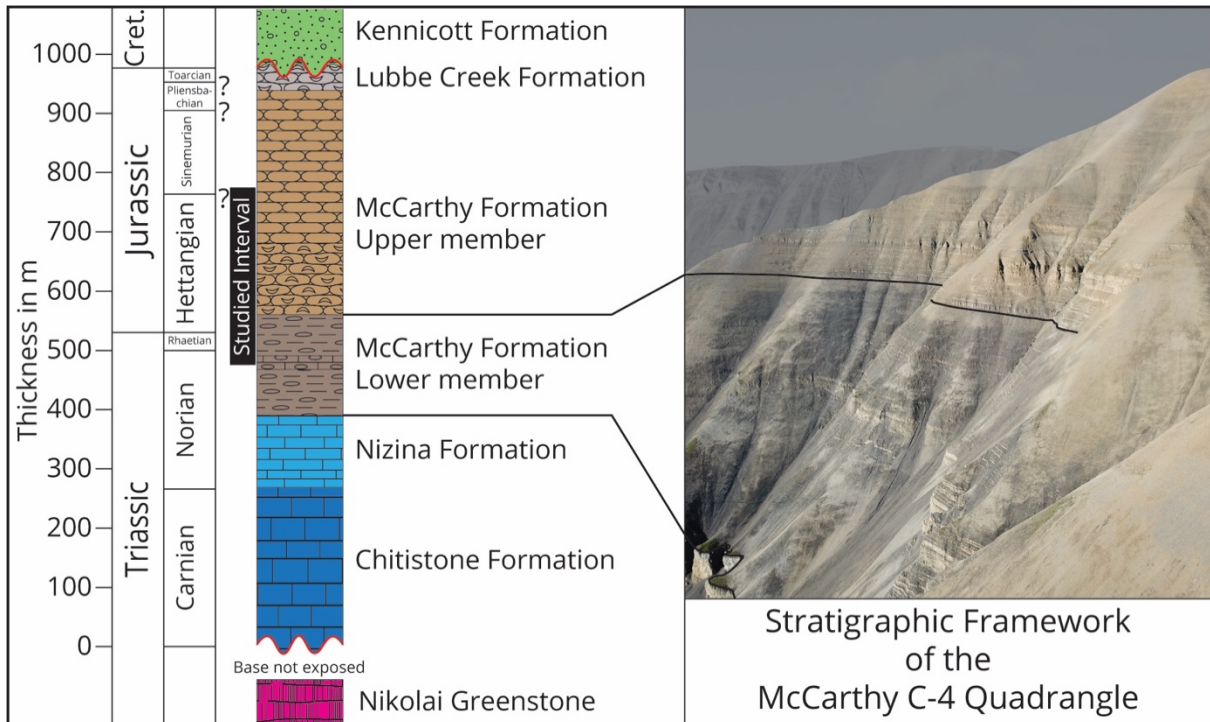
Figure 1: Stratigraphic framework of the Triassic-Jurassic of the Wrangell Mountains, based on MacKevett (1970a); Trop et al. (2002); Witmer (2007); Caruthers et al. (2021). The photograph is taken towards the south and shows part of the Grotto Creek section. The member boundary of the McCarthy Formation is marked by a color change in the landscape. On a smaller scale, the McCarthy Formation shows alternations between cliff-forming and slope-forming intervals, which correspond to the facies associations of this study.

mapping campaigns (MacKevett 1963; 1970a; 1970b; 1972; 1974; 1978; 1978; MacKevett and Smith 1972a; 1972b; Winkler and MacKevett 1981). More recently, the McCarthy Formation was placed in context of the evolution of the volcanic terrane of Wrangellia (Trop et al. 2002; 2007). The formation has been interpreted to represent the distal environments of a ramp that submerged below storm wave-base during post-volcanic subsidence following the deposition of the more proximal Chitistone and Nizina Formations (Armstrong, MacKevett, and Silberling 1969; Witmer 2007). Yet, the sedimentology and stratigraphy of the McCarthy Formation has not been extensively researched.

Distal ramp records like the McCarthy Formation can record shallow-water trends because shallow-water sediment can be reworked and deposited in environments situated below storm wave-base (e.g. Puga-Bernabéu et al. 2014), which are referred to as the outer ramp (Burchette and Wright 1992). In facies models, the outer ramp is often presented as a wide facies belt where sedimentation occurs mostly through the vertical settling of hemipelagic sediment, with rare reworking by turbidity currents and storms (Burchette and Wright 1992; Schlager 2005). However, even though reworking may be rare, reworked sediments are well-represented in outer ramp records (e.g. Slootman et al. 2016). Sugisaki, Yamamoto, and Adachi (1982) recognized early on that deepwater cherts, for example, are not exclusively pelagic oozes, but may have been reworked. More recent studies on the sedimentology of ancient ramps link the products of reworking to storms, turbidity currents, and mud and debris flows (e.g. Payros et al. 2010; Puga-Bernabéu et al. 2014; Pomar et al. 2019), as well as bottom currents (e.g. Puga-Bernabéu et al. 2010; Reolid, Betzler, and Lüdmann 2019). As a result of these processes, the outer ramp can record biogeochemical changes in shallower waters.

The aim of this project was to analyze the facies and architecture of the McCarthy Formation at Grotto Creek in order to reconstruct (1) its outer ramp depositional environments and (2) the biogeochemical regime of sediment production in shallower waters from the Late Triassic to Early Jurassic.

The McCarthy Formation records the reworking of biogenic sediment from shallow waters to outer ramp lobe complexes. When the supply of
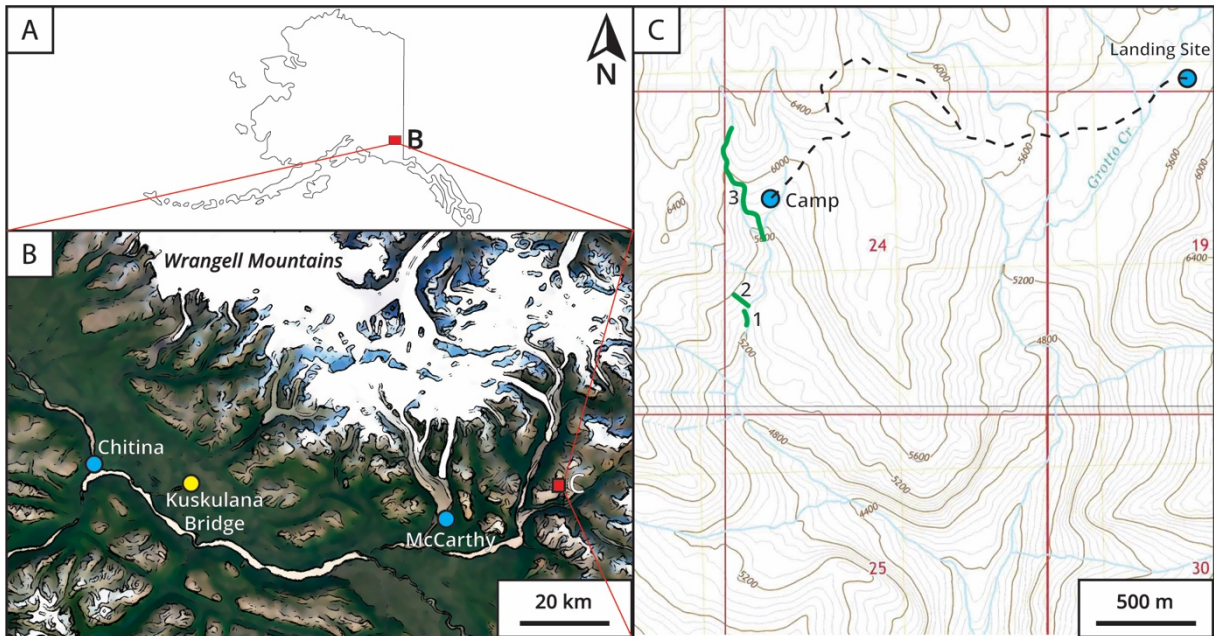
Figure 2: Location of the Grotto Creek section relative to A) Alaska, B) the Chitina River Valley, and C) Chitistone Mountain. C) The dotted line is the hiking route from the landing site at Grotto Creek to the section. The green lines mark the three sub-sections of this study. Basemap: USGS non-ortho US Topo 2017.

reworked sediment was reduced, background sedimentation predominated. Biosiliceous sediment production increased in the Hettangian, when the siliceous carbonate-ramp transitioned to a glass ramp. This transition was associated with an order of magnitude increase in sedimentation rates, which shows how an increase in sediment production in the shallows can increase the sediment supply to the outer ramp.

2. Materials and methods

2.1 Fieldwork

The McCarthy Formation (fig. 1) was studied during two field campaigns in 2017 and 2019 at the Grotto Creek section in Wrangell-St. Elias National Park and Preserve in the southeast of Alaska (fig. 2). I joined a team of 9 earth scientists during the 2019 field campaign. We flew from the town of McCarthy to the headwaters of Grotto Creek and hiked to the tributary where the section is located. We studied ~290 m of stratigraphy, which includes the upper part of MacKevett's (1963; 1978) lower member and the lower part of the upper member (fig. 1).

We measured, described, and sampled three sub-sections (fig. 2). The lower section (base at 07V 423 246 m, 6 819 740 m) is 26.28 m thick and was studied along the creek. The top of the lower section is a ~0.5 m thick dolerite sill, which also forms the base for the middle section (07V 423 251 m, 6 819 839 m). The middle section is 70 m thick and was studied by climbing the slope. The uppermost ~34 m of this section overlaps with the upper section. We correlated these two sub-sections using prominent marker beds. The upper section is ~227 m thick and was studied along the creek (from 07V 423 340 m, 6 820 172 m to 423 156 m 6 820 894 m).

2.2 X-Ray diffraction

All laboratory work was carried out at Utrecht University. I determined the bulk mineralogy using X-ray diffraction (XRD) on 52 random powders. First, the samples were crushed using a Herzog HP-MA for 60 seconds. The

powders were then mounted in sample holders with a diameter of 25 mm. I used a Bruker d8 Advance diffractometer using Cu-Kα radiation at 40 kV and 40 mA. The diffractometer scanned the samples from 3° to 75° 2θ in increments of 0.020°. During the measurement, the sample rotated at 0.25 Hz. I used a variable divergence slit opening to ensure fixed sample illumination with an irradiated length of 20 mm. The diffractograms were interpreted using the EVAL Suite software by Bruker.

2.3 X-ray fluorescence

I analyzed the bulk elemental composition of 35 samples using X-Ray Fluorescence (XRF). Each sample (~10 g) was powdered for 120 seconds by the Herzog HP-MA and pressed into tablets with a diameter of 35 mm by the Herzog HP-PA. The bulk elemental composition was measured by the ARL Perform'X. The sum of the wt% of the major elements (Al_2O_3, CaO, Fe_2O_3, K_2O, MgO, MnO, Na_2O, P_2O_5, SiO_2, and TiO_2) was on average ~84%/100% (see Appendix D).

2.4 Grain size analysis

I analyzed the grain size of the insoluble residue of 29 samples from the lower member. The samples are siliceous, which hindered rock disaggregation. The samples were therefore first crushed to coarse sand using a hammer. Then, the samples were placed in beakers with 3M HCl and magnetic stirring rods at 70°C for 4 days. After I neutralized the remaining acid, the samples were placed in 12% H_2O_2 and were continuously stirred while the organic matter
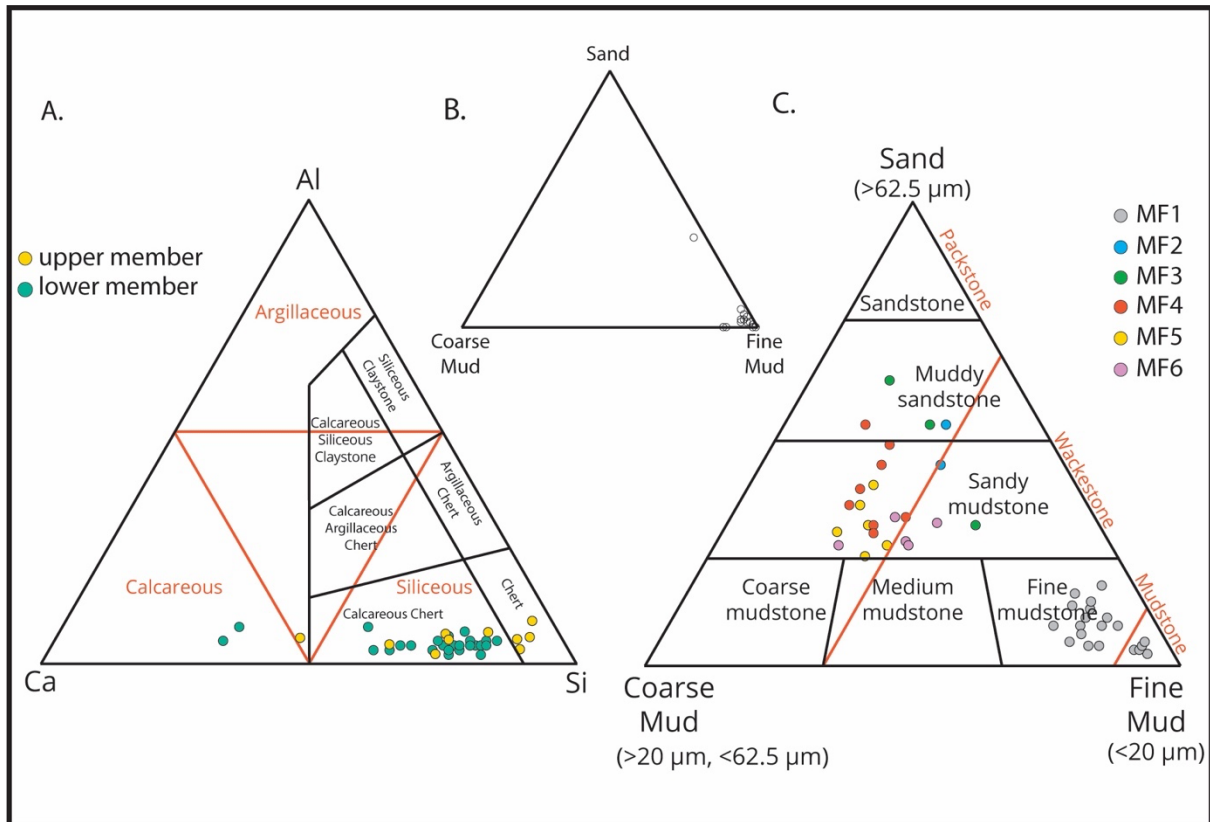
Figure 3: The facies of the McCarthy Formation in three ternary diagrams. A) Compositional ternary diagram combining Lazar et al. (2015) (in red) and Jones and Murchey (1986) (in black). Most samples are siliceous mudstone and calcareous chert. The calcareous samples are rich in shell fragments and only occur in the lower member, whereas bedded cherts are often spiculitic and only occur in the upper member. The Al% is low, which shows that the total lithogenic component is small. B) Grain size ternary diagram. Most of the insoluble residue is microcrystalline. C) Textural ternary diagram combining a modification of Lazar et al. (2015) (in black, see also section 2) with Dunham (1962) (in red). The mudstone-wackestone boundary corresponds to 90% fine mud, and the wackestone-packstone boundary is placed at 35% fine mud, the approximate upper limit for grain-supported fabrics.

oxidized. When the reaction had visibly ceased, the samples were heated to 90°C to allow any remaining H_2O_2 to react.

I dispensed the samples in the Malvern Hydro 2000G dispersion unit and added 25 mL of the dispersing solution (44.6 g $Na_4P_2O_7 \bullet 10H_2O$ and 4.24 g Na_2CO_3 in 1 L deionized H_2O). Before the measurement, I applied 60 seconds of ultrasonication with a maximum tip displacement of 4 μm. The grain size was measured from 0.02 μm to 2 mm by the Malvern Mastersizer 2000, using a refractive index of 1.544 and an absorption index of 0.9. I made

three duplicate measurements, which showed that the machinery operated consistently, and that there was no significant bias in subsampling and dispensing the sample (Appendix E).

2.5 Petrography and microfacies

For 44 samples, thin sections were made and scanned using a Leica M165C stereomicroscope. The thin sections were studied in plane-polarized and cross-polarized light using a Zeiss Axio optical microscope and photographed by the Zeiss Axiocam 305 Color camera. Reflected light was applied to determine the composition of opaque materials.

Because many of the samples are fine-grained, I adopted an approach that was modified from Lazar et al. (2015) to adequately capture the textural variability. I defined fine mud as grains smaller than 20 µm and coarse mud as grains between 20 and 62.5 µm. The reason for this modification is that 20 µm corresponds to the average thickness of the thin sections. As a result, grains smaller than 20 µm have a darker appearance under the microscope, which sets them apart from coarser grains. Coincidentally, 20 µm is the boundary between mud and grains in the Dunham classification (Dunham 1962).

I estimated the fine mud, coarse mud, and sand fractions using ImageJ by Fiji software. I used stereomicroscope scans for this analysis, as this allowed me to capture relatively large and representative areas of the thin sections. The resolution of these scans is ~7 µm/px. First, grains with an area smaller than 4 pixels were excluded to avoid noise, which corresponds to
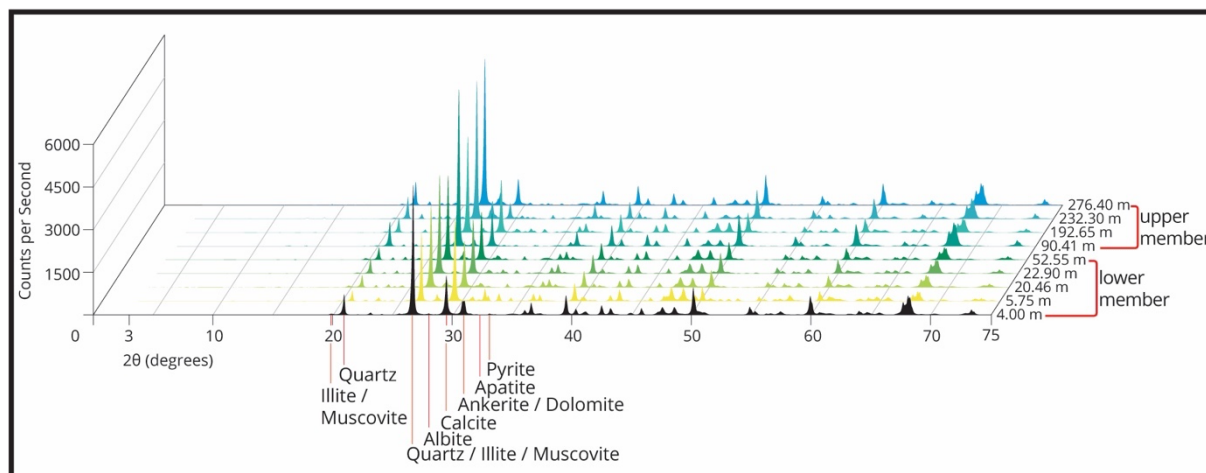
Figure 4: XRD diffractograms of 9 representative samples of the studied interval. The samples show that the mineralogical composition, qualitatively speaking, is monotonous. In general, the quartz/calcite intensity ratio is higher in the upper member, which indicates that the upper member is more siliceous than the lower member.

grains with a nominal diameter of 19.7 µm or finer. Secondly, I used a brightness threshold to differentiate fine mud and coarser grains, which resulted in a binary image that included all grains that were coarser than 20 µm. This binary image was then filtered to differentiate coarse mud (>20 µm, <62.5 µm) and sand grains (>62.5 µm).

I didn't use the brightness threshold for samples with a lot of carbonate cement, because the cement and the grains have a similar brightness under the microscope. For these samples, I assessed the grain size distribution by comparing them to other samples and to visual charts (Baccelle and Bosellini 1965).

In the microfacies descriptions, I adopted the semi-quantitative terminology of Macquaker and Adams (2003): dominating (>90%), rich (50-90%), and bearing (10-50%). To quantify the intensity of bioturbation, I used the ichnofabrics index by Droser and Bottjer (1986). To describe the thickness of beds and laminae, I used the terminology adapted from Campbell (1967).

3. Results

The facies of the McCarthy Formation (fig. 3, 4) were characterized, and its stratigraphy (fig. 5) was subdivided into four facies associations (table 1; fig. 6–10). The thin sections (N=44) were subdivided into nine main microfacies (table 2; fig 11–18). I also calculated approximate sedimentation rates for the Rhaetian and Hettangian at Grotto Creek (table 3) and constructed isopach maps based on existing literature (fig. 19).

3.1 Facies characterization

The facies of the McCarthy are siliceous (fig. 3A): The appropriate name for most samples (N=29) is siliceous mudstone (sensu Lazar et al. 2015) and calcareous chert (sensu Jones and Murchey 1986; fig. 3A). There are a couple of calcareous samples (N=2) and a few (N=4) are siliceous enough to be named chert (fig. 3A). Calcareous samples are rich in sparite cement (e.g. fig. 17F), shell fragments (e.g. fig. 14), or calcispheres (e.g. fig. 16), whereas siliceous samples contain radiolarians (e.g. fig. 13E) or spicules (e.g. fig. 13G; fig. 17). In addition, microcrystalline quartz is an important siliceous phase in the McCarthy Formation, which is shown by fine textures of the insoluble residue of samples from the lower member (fig. 3B): out of 29 samples, 26 have a grain size mode below 5 μm.

Overall, the upper member is more siliceous than the lower member: (1) Bedded cherts are only present in the upper member (fig. 3A). In the lower member, chert occurs only in nodules; (2) In general, the quartz/calcite XRD
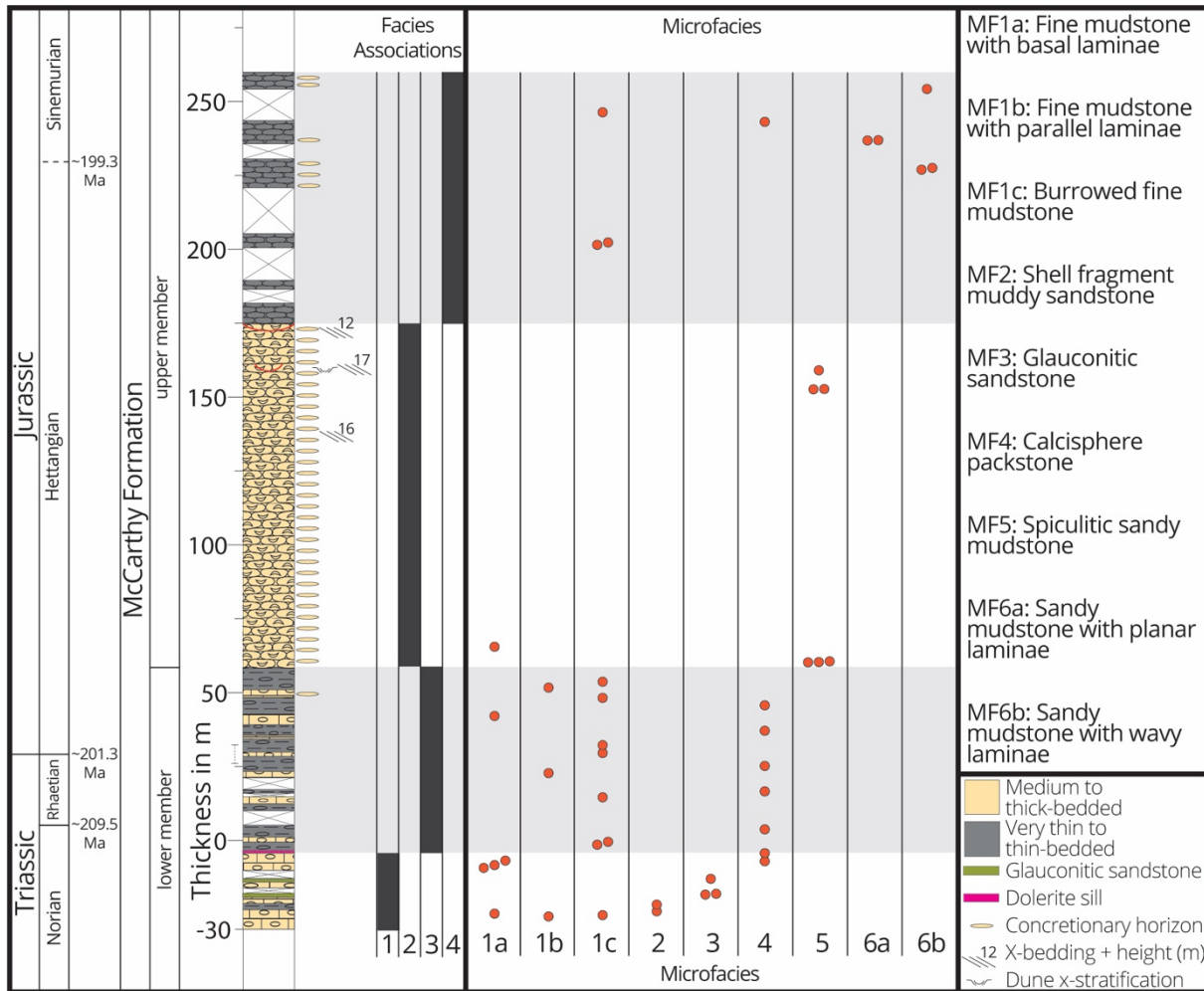
Figure 5: Schematic log of the studied interval, which shows an alternation between cliff-forming thicker-bedded intervals (FA1 and FA2), interpreted as lobe complexes, and slope-forming thinner-bedded intervals (FA3 and FA4; grey shading), interpreted as sediment-starved outer ramp environments. The upper member is more siliceous than the lower member. The Rhaetian is condensed at Grotto Creek, whereas the Hettangian is more expanded (see also Table 3; Caruthers et al. 2021).

intensity ratio is higher in the upper member than in the lower member (fig. 4); (3) In thin section, the upper member has a higher abundance of siliceous spicules (fig. 17), whereas the lower member contains more calcareous shell fragments (fig. 14).

Beside quartz and calcite, the typical mineralogical assemblage of the McCarthy Formation consists of albite, apatite, pyrite, dolomite, ankerite, hematite, and muscovite (fig. 4). The total amount of Al in the rocks is low (fig. 3A), which shows that the lithogenic component is small.

3.2 Facies associations

The four facies associations in the studied interval are described below and summarized in Table 1.

Table 1: Overview of the facies associations of the McCarthy Formation.

		Facies Associations	Description	Common Microfacies		Environment
Cliff-forming	lower member	FA1	Medium to thick-bedded siliceous mudstones, calcareous cherts, shell-fragment limestones, and very thin to thin partings.	MF1a	Fine mudstone with basal laminae	Siliceous carbonate-ramp lobe complex
				MF2	Shell fragment muddy sandstone	
				MF3	Glauconitic muddy sandstone	
	upper member	FA2	Medium to thick-bedded spiculitic cherts and concretionary horizons.	MF5	Spiculitic sandy mudstone	Glass ramp lobe complex
Slope-forming	lower member	FA3	Thin-bedded and subordinately thick-bedded siliceous mudstones, calcareous cherts, and limestones.	MF1b	Fine mudstone with parallel laminae	Sediment-starved outer ramp of a siliceous carbonate-ramp
				MF1c	Burrowed fine mudstone	
				MF4	Calcisphere packstone	
	upper member	FA4	Thin to medium-bedded siliceous mudstones alternating with medium to thick-bedded laminated calcareous cherts.	MF1c	Burrowed fine mudstone	Sediment-starved outer ramp of a glass ramp
				MF4	Calcisphere packstone	
				MF6a	Sandy mudstone with planar laminae	
				MF6b	Sandy mudstone with wavy laminae	

Table 2: Descriptions of the microfacies of the McCarthy Formation. See also appendix A. BI: Bioturbation Index (Droser and Bottjer 1986).

Microfacies	Subdivision	Code	Occurs in	Textures	Field Lithofacies	Sedimentary Structures	BI	Interpretation
Fine Mudstone Dunham: Mudstone/ Wackestone;	With basal laminae	**MF1a** N = 6 fig. 11	FA1 Subordinate in FA2, FA3	Dominated by fine mud (~70-95%). Coarser grains are coarse mud to medium sand-sized grains of sub-angular quartz and calcite. Some sand grains are recognizable as radiolarians, calcispheres, or foraminifera. A few samples contain carbonate concretions that are rich in sand-sized peloids.	Medium grey to black siliceous mudstones and calcareous cherts, some of which are very thin to thin-bedded, forming thin to medium bedsets, whereas others are medium to thick bedded. Beds of this microfacies are sometimes laminated.	Very thin continuous and discontinuous basal laminae and asymptotic cross-laminae. Grading.	2	Reworking by turbidity currents
	With parallel laminae	**MF1b** N = 3 fig. 12	FA1, FA3			Very thin to thin parallel laminae without basal scours.	2	Suspension settling from water column.
	Burrowed	**MF1c** N=11 fig. 13	FA1, FA3, FA4			-	5-6	Suspension settling, turbidity currents, debris flows (see 4.1 for discussion).
Shell fragment muddy sandstone Dunham: Packstone		**MF2** N=2 fig. 14	FA1	Rich in thin calcareous shell fragments (50-60%). The rest of the fabric consists of coarse mud-sized calcite grains and peloids, and fine mud. Contains a few bryozoans.	Thin to thick beds of grey indurated sandy limestones.	-	4	Reworking.
Glauconitic muddy sandstone Dunham: Grainstone/ Packstone/Wackestone		**MF3** N=3 fig. 15	FA1	Characterized by well-rounded fine to medium sand that consists of glauconite. The glauconite grains are glauconitized fecal pellets and microfossils. Bears fine mud, shell fragments, and coarse mud to sand-sized grains of sub-angular calcite and contains few spicules.	Dark, medium to thick beds of glauconitic sandstone. One bed is a glauconitized packstone of *Heterastridium*.	-	5	Reworking, *in situ* glauconitization.
Calcisphere packstone Dunham: Packstone		**MF4** N=8 fig. 16	FA3, FA4, Subordinate in FA1	Characterized by coarse mud and sand fractions (70-90%) that are dominated by calcispheres. Well-cemented and bears fine mud.	Thin to thick beds of sandy limestone and calcareous chert. Often indurated and concretionary.	-	5	Suspension settling from pelagic blooms.
Spiculitic sandy mudstone Dunham: Packstone		**MF5** N=6 fig. 17	FA2	Characterized by coarse mud and sand fractions (>70%) that are rich in spicules. This microfacies occurs in cherts (more siliceous mud) and concretions (more sparite). Also contains echinoid fragments, radiolarians, calcispheres, foraminifera.	Medium to thick beds of dark chert and buff-colored concretionary horizons.	Some concretionary beds contain dune cross-stratification.	5	Reworking, winnowing by bottom currents.
Laminated sandy mudstone Dunham: Packstone	With planar laminae	**MF6a** N=2 fig. 18	FA4	Characterized by coarse mud and sand fractions (>68%) of sub-angular calcite that is concentrated in well-cemented laminae. Contains calcispheres. Bears shell fragments and organic material.	Medium to thick buff-colored beds of calcareous chert. Sometimes concretionary.	Bigradational sorting within the same beds. In thin section, coarsest part contains very thin planar parallel laminae, finer parts contain basal fining-upwards laminae and sigmoidal cross-laminae.	1	Reworking by contour currents.
	With wavy laminae	**MF6b** N=3 fig. 18	FA4			Very thin wavy laminae that are sometimes draped by organic material.	1	Microbial mat colonization

Figure 6: Facies association 1, interpreted as an outer ramp lobe complex on a siliceous carbonate-ramp. A) Photograph taken towards south-west. FA1 is cliff-forming and appears to pinch towards the south, which is interpreted to represent the geometry of the lobe complex. (B–C) FA1 consists of medium to thick beds and thin partings. Thicker beds sometimes contain sand-sized shell fragments (MF2) or glauconite (MF3). B and C show the same bedset: The bed thickness changes laterally over ~10 m, which is interpreted to represent the geometry of lobe elements. D) Laminated bed with irregular basal contacts, consisting of fine mudstone with basal laminae (MF1a).

3.2.1 FA1: Cliff-forming succession of medium to thick-bedded siliceous mudstones, calcareous cherts, shell-fragment limestones, and very thin to thin partings (fig. 6).

Part of the lower member of MacKevett (1963).

A ~26 m thick cliff-forming succession with medium to thick beds of siliceous mudstone, calcareous chert and limestone. These beds are indurated and separated by partings of fissile mudstone (fig. 6). The contacts between beds are sharp and can be slightly irregular (fig. 6D). Both the partings and most thicker beds are medium grey to black when fresh and consist of very thin to thin beds of siliceous fine mudstones (MF1). Some of these fine

mudstones have very thin basal laminae (MF1a; fig. 11), whereas others are burrowed (MF1c; fig. 13). Nodules of chert and apatite are common within the siliceous mudstones (fig. 11A). Some thin to thick beds are coarser and contain sand-sized shell fragments (MF2; fig. 14) or glauconite (MF3; fig. 15). Common megafossils are *Monotis*, *Heterastridium,* and ammonites (see also Caruthers et al. 2021). The thickness of a bedset was observed to change laterally over a distance of ~10 m (fig. 6B, C). On a larger scale, FA1 appears to pinch towards the south in the Grotto Creek section (fig. 6A).

3.2.2 FA2: Cliff-forming succession of medium to thick-bedded spiculitic cherts and concretionary horizons (fig. 7, 8).

Part of the upper member of MacKevett (1963).

A ~120 m thick cliff-forming succession of medium to thick-bedded dark spiculitic chert and buff-colored carbonate concretionary horizons (fig. 7). The concretionary horizons and the cherts are similar in texture, as both the cherts and the concretions consist of spiculitic sandy mudstone (MF5; fig. 17). The difference between the cherts and concretionary horizons is that the cherts contain more siliceous mud (fig. 17G), whereas the concretions contain more sparite (fig. 17E). The concretions are ~30 cm thick and have a horizontal diameter of ~60 cm. They often coalesce laterally to form continuous horizons with wavy contacts (fig. 7B). In several concretionary horizons, we observed sigmoidal surfaces that downlap asymptotically onto the underlying bedding plane (fig. 7C).
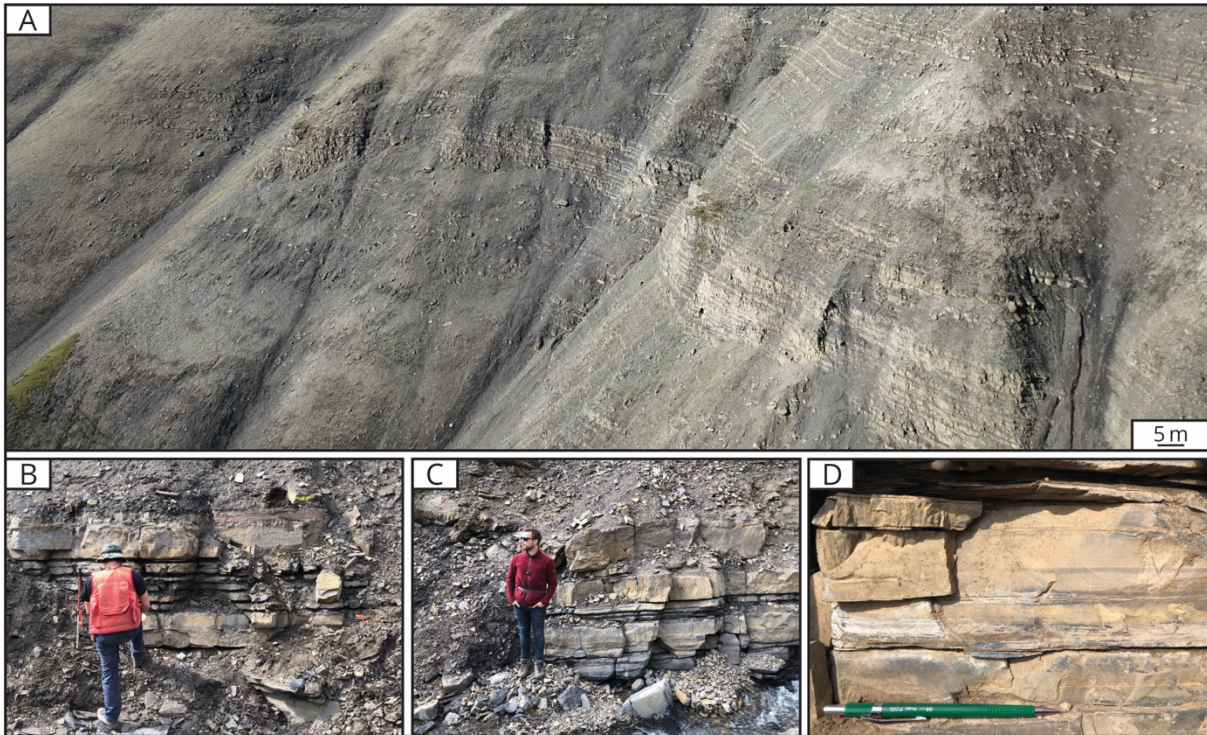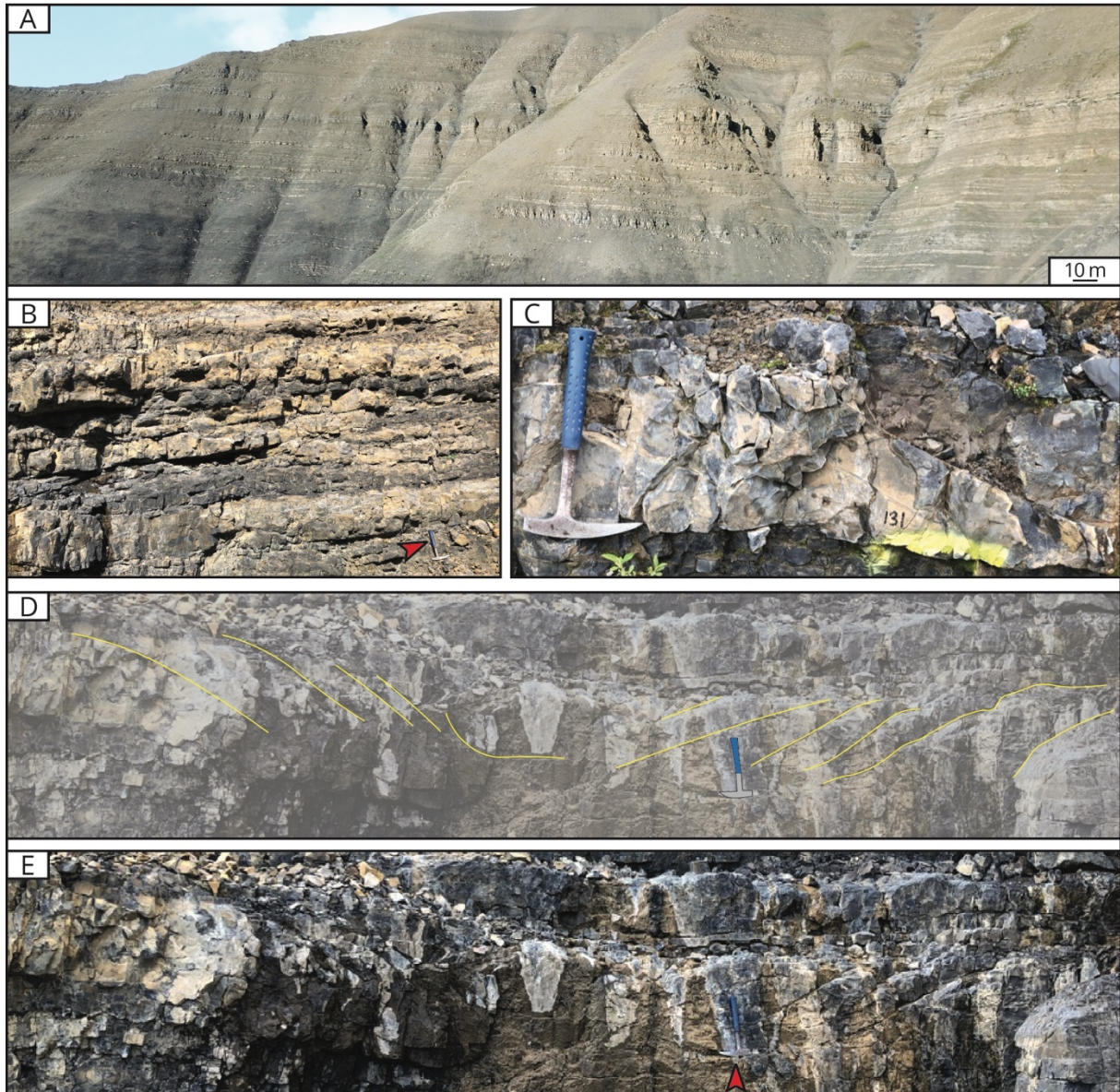
Figure 7: Facies association 2, interpreted as an outer ramp lobe complex on a glass ramp. A) Photograph taken towards the west. (B) FA2 consists of dark spiculitic chert and buff spiculitic concretionary horizons (both MF5). Red arrow marks hammer for scale. C) Sigmoidal cross-stratification that downlaps towards the right onto the bedding plane, interpreted as dune cross-stratification. (D–E) Set of cross-stratification that represents dune migration directed away from the camera. Red arrow marks hammer for scale.

The uppermost ~50 m of FA2 show sets of large-scale cross-stratification with heights of 12–17 m and dip angles of 6–8 degrees (Heinhuis 2020; fig. 6). The concretions in the intervals with large-scale cross-stratification are ~8 cm tall and 10–20 cm wide, which is smaller than in the rest of FA2 (fig. 8). The sets of cross-stratification are associated with

channelforms with a depth of ~3 m and a width of ~15 m (Fig. 8A). The channelforms cut into the sets of large-scale cross-stratification and, in turn, are filled by cross-stratification (fig. 8A). The upper boundary of FA2 is an erosional surface with larger channelforms that have a depth of 5–10 m and a width of ~30 m (fig. 8C).

3.2.3 FA3: Slope-forming succession of thin-bedded and subordinately thick-bedded siliceous mudstones, calcareous cherts, and limestones (fig. 9).

Part of the lower member of MacKevett (1963).

A ~70 m thick slope-forming succession that is predominated by dark thin-bedded siliceous fine mudstones, which contain parallel laminae (MF1b; fig. 12) or burrowed fine mudstone (MF1c; fig. 13). The medium to thick beds are buff-colored and consist of calcisphere packstones (MF4; fig. 16) and subordinately of siliceous fine mudstones (MF1b; fig. 12 or MF1c; fig. 13). Some of the fine mudstones contain small (~1–2 cm in diameter) carbonate concretions or chert nodules, which are internally rich in sand-sized peloids (fig. 12B). In the upper ~40 m of FA3, both the thin-bedded and thick-bedded strata are sometimes laminated. A few siliceous mudstones in the upper part of FA3 bear outsized shell fragments or plant material (see also Witmer 2007). The contacts between the different beds can be sharp and gradational. FA3 also contains several ash layers (see Caruthers et al. 2021). The base of FA3 contains several syn-depositional folds with a maximum height of ~12 m (fig. 9B).
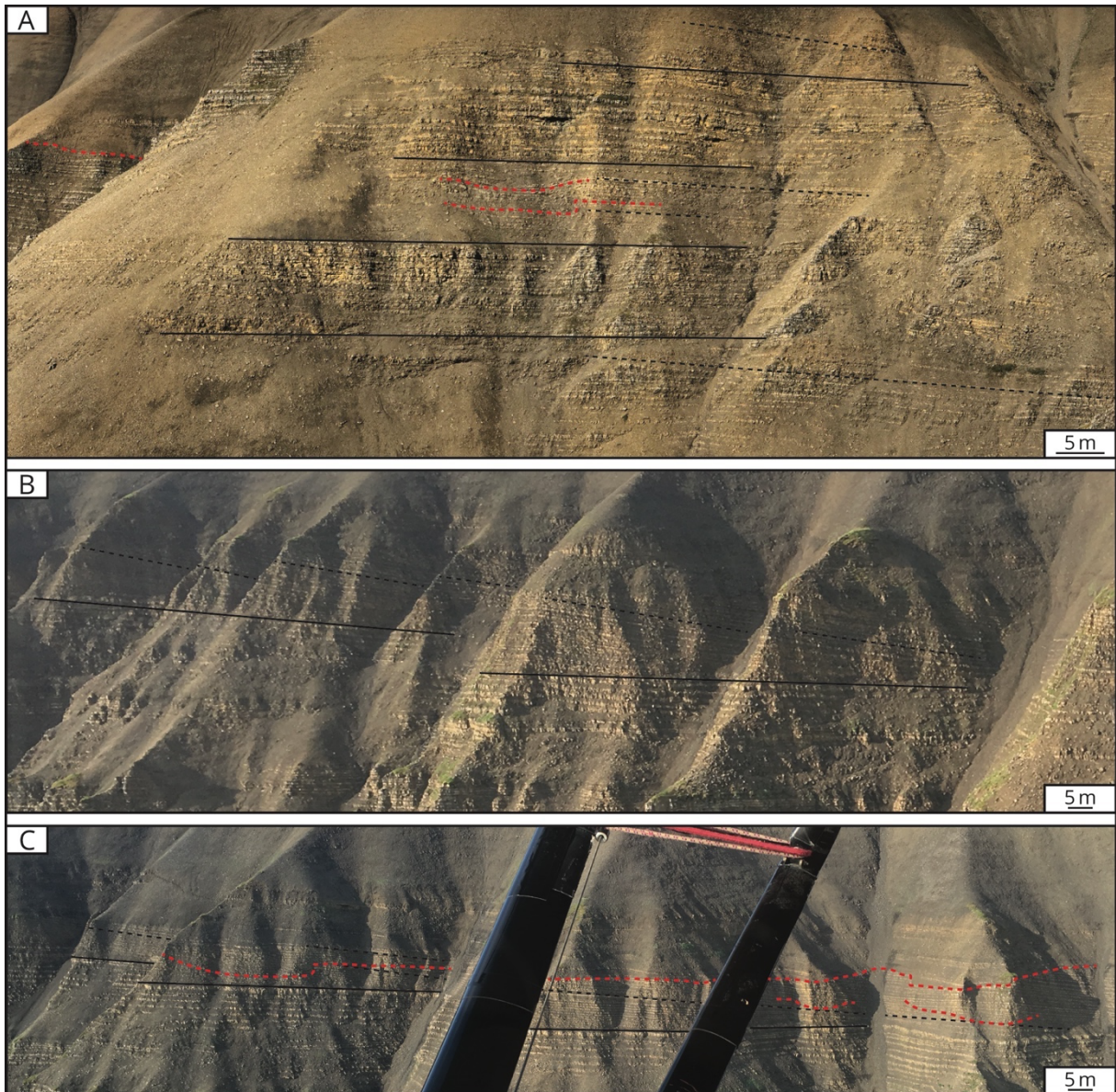
Figure 8: The large-scale architectural elements of FA2, interpreted as a bottom current-induced sediment drift. Continuous black lines mark horizontal stratification, dotted black lines mark cross-stratification and the dotted red lines mark channelforms. The sets of cross-stratification have a heights of 10–17 m and corrected dip angles of 6–8 degrees (Heinhuis 2020). (A) is photographed towards the west in the Grotto Creek section. (B–C) are photographed towards the southwest from a plane about 2 km west of the Grotto Creek section.

3.2.4 FA4: Slope-forming succession of very thin to medium-bedded siliceous mudstones alternating with medium to thick-bedded laminated calcareous cherts (fig. 10).

Part of the upper member of MacKevett (1963).

An ~85 m thick slope-forming succession of very thin to medium-bedded siliceous mudstones, that have a black to dark olive color (fig. 10B), consist of MF1c (burrowed; fig. 13), and are typically richer in chalcedony than the mudstones of the lower member of the McCarthy Formation. The upper half of FA4 also contains indurated medium to thick beds that appear every 1 to 10 m (fig 10A). These thicker beds are buff-colored calcareous cherts that consist of laminated sandy mudstone (MF6; fig 18) and are sometimes concretionary. Some of these thicker beds exhibit bigradational sorting – a vertical transition of reverse to normal grading within the same bed (fig. 10C; MF6a; fig. 18A). Other thicker beds contain very thin wavy laminae (MF6b; fig. 18G). FA4 contains several ash layers.

Table 3: Thicknesses and approximate sedimentation rates for the Rhaetian and the Hettangian of the Grotto Creek section. The linear sedimentation rate was substantially higher in the Hettangian than in the Rhaetian, even when considering decompaction and a short Rhaetian stage. The Norian – Rhaetian boundary and the Rhaetian – Hettangian boundary were identified by Caruthers et al. (2021). The Hettangian-Sinemurian boundary is provisionally placed at 235.7 m, corresponding to the first occurrence of a Sinemurian ammonite in float, namely *Agassiceras* cf. *scipionianum* (Caruthers pers. comm.). For decompaction, I used the mean curves for porosity loss for shales and carbonates by Kim, Lee, and Lee (2018).

Stage	Position of boundaries	Thickness	Duration	Average Sedimentation Rate	
				Compacted	Decompacted
Rhaetian	3.7 m – 31.2 m	27.5 m	~4 Ma	~7 m/Ma	~17 m/Ma
			~8 Ma	~3 m/Ma	~8 m/Ma
Hettangian	31.2 m – 235.7 m	204.5 m	~2 Ma	~100 m/Ma	~200 m/Ma
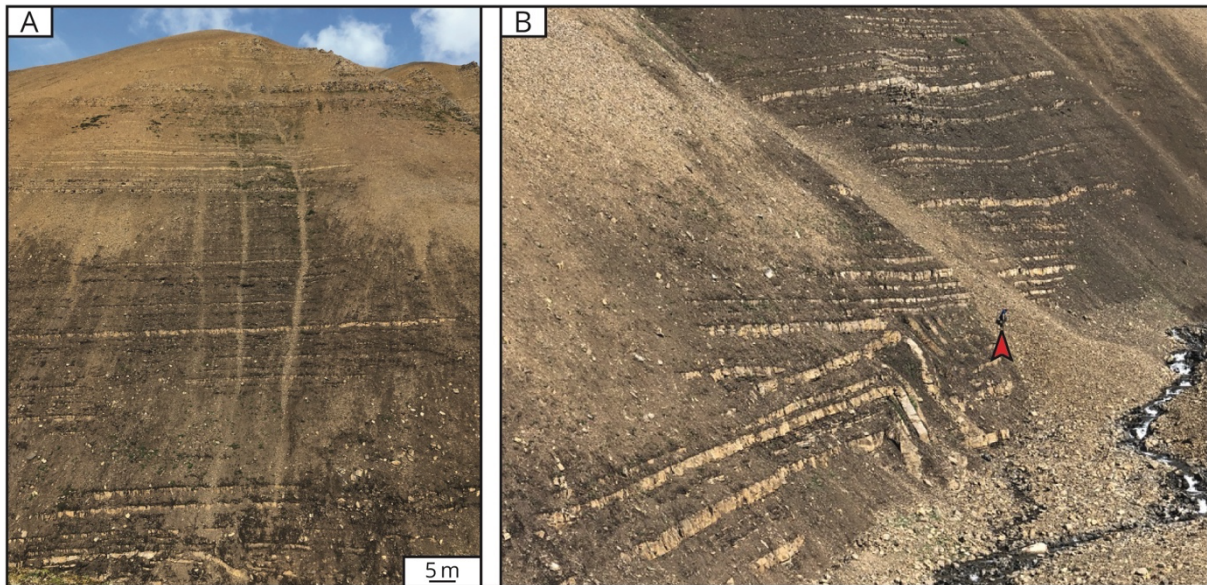
Figure 9: Facies association 3, interpreted as a sediment-starved outer ramp environment on a siliceous carbonate-ramp. A) Photograph taken towards the west. FA3 is slope-forming and consists mostly of thin beds of burrowed fine mudstone (MF1c). There more prominent, thicker beds that typically consist of calcisphere packstones (MF4). (B) A syn-depositional folding structure interpreted as a slump. Red arrow marks person for scale.

4. Microfacies interpretations

The microfacies of this study (fig. 10–18) are described in Table 2 (see also Appendix A) and are interpreted below.

4.1 MF1: Fine mudstone

The beds of fine mudstone with basal laminae (MF1a; fig. 11) are interpreted as fine-grained turbidites: MF1a represents waning flows that eroded the substrate to produce basal scours, and subsequently deposited basal laminae, cross-laminae, and graded or structureless fine mud. As the sharp basal scours of MF1a reflect erosion, they are bedding planes that separate very thin beds (fig. 11E). The scours and silt laminae of MF1a resemble those from other studies that are associated with bedload transport (Schieber, Southard, and Thaisen 2007; Schieber and Southard 2009; Yawar and Schieber 2017).

In contrast to MF1a, the laminae in MF1b (fine mudstone with parallel laminae; fig. 12) are not associated with scours, which shows that the peak flow velocity wasn't high enough to erode the substrate. Therefore, the mud that forms MF1b is interpreted to have settled from suspension.

The burrowed fine mudstone (MF1c; fig. 13) may reflect a variety of processes that, due to the burrowing, are difficult to reconstruct. However, some of the burrowed fine mudstones bear calcispheres (fig. 13), which indicates deposition by suspension settling from the water column. There are also indications that some beds of MF1c are the product of more dynamic processes, like turbidity currents or debris flows: (1) The burrowed fine
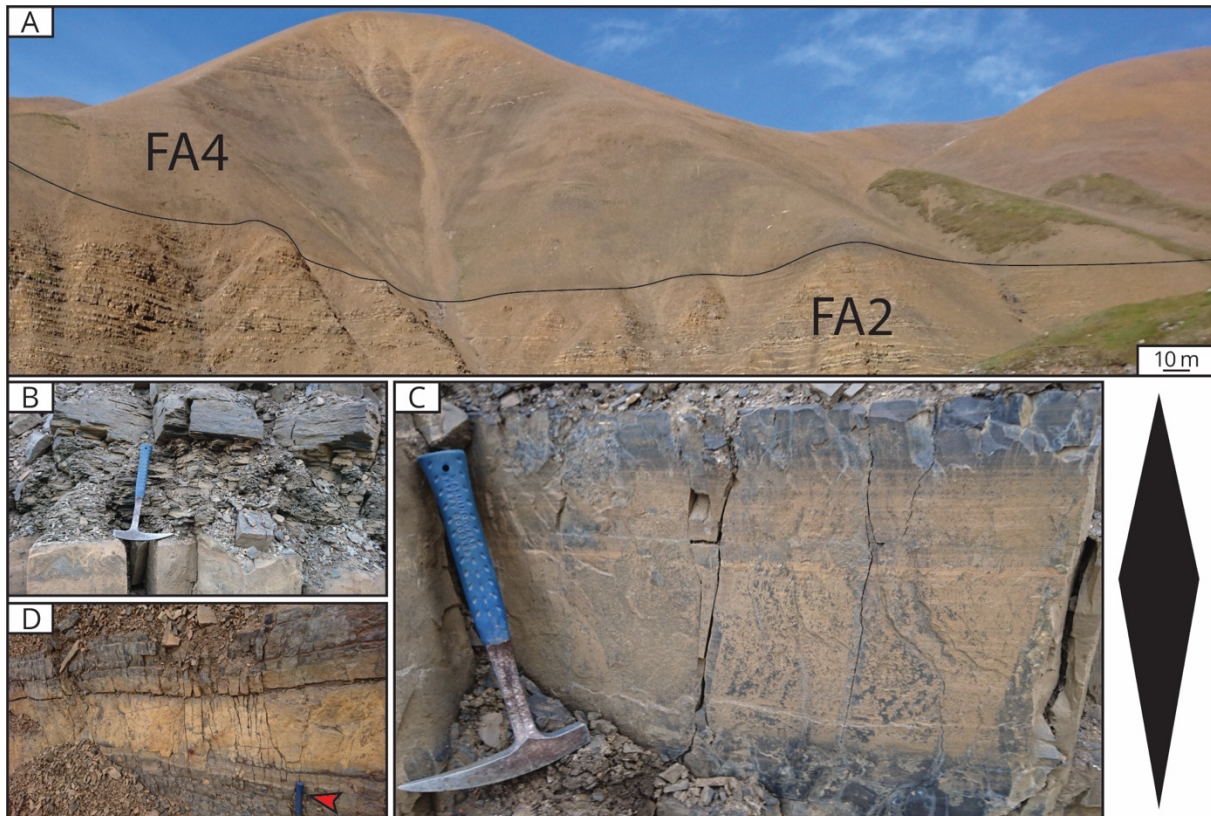
Figure 10: Facies association 4, interpreted as a sediment-starved outer ramp environment on a glass ramp. (A) Photograph taken towards the west. FA4 is slope-forming, although the upper half of FA4 also contains prominent beds. (B) Most beds are thin and consist of burrowed fine mudstone (MF1c). (C) Some of the thicker beds show bigradational sorting and are interpreted as contourites (MF6a). (D) Some thicker beds are horizons of coalesced concretions, that can represent contourites (MF6a) and microbial mat colonization (MF6b).

mudstones often contain *Phycosiphon* sp. (fig. 13B)*,* which is linked to early colonization following rapid sedimentation events (e.g. Rodríguez-Tovar, Nagy, and Reolid 2014). (2) The sand-sized peloids that were preserved in carbonate concretions of several fine mudstones (fig. 12B) show that the primary texture of the mud was peloidal. Peloids can be transported in bedload (Schieber et al. 2013; Birgenheier and Moore 2018); 3) Some of the fine mud is associated with outsized clasts, such as shell fragments and plant material in FA3 (see also Witmer 2007). In conclusion, the burrowed fine mudstones of the McCarthy Formation can represent background sedimentation, but also more dynamic processes.

4.2 MF2: Shell fragment muddy sandstone

The broken bioclasts show that beds of this microfacies (MF2; fig. 14) represent reworked deposits. The high intensity of bioturbation makes it difficult to recognize sedimentary structures, and therefore the depositional process behind the reworking remains unclear. The deposition of beds of this microfacies likely occurred in an episodic manner, as the presence of *Phycosiphon* sp. (fig 14F) is often associated with event deposits (e.g. Rodríguez-Tovar, Nagy, and Reolid 2014).

4.3 MF3: Glauconitic sandstone

The glauconitic sandstone (MF3; fig. 15) represents multiple depositional processes in a chemical environment that was suitable for *in situ* glauconitization. The uniform size and well-rounded shape of the glauconite grains indicate that the majority are glauconitized fecal pellets. Fecal pellets can form *in situ*, but can also be transported over long distances (Schieber 2016). The association of these pellets with reworked clasts, like shell fragments (fig. 15B), suggest that the fecal pellets were reworked. Other glauconite grains formed in foraminifera tests (fig. 15F, G) or in *Heterastridium*, which is a hydrozoan with a planktonic lifestyle (Schäfer and Grant-Mackie 1998) that represents pelagic sedimentation. The fact that glauconitization occurred in both reworked and pelagic clasts shows that glauconitization occurred *in situ*.
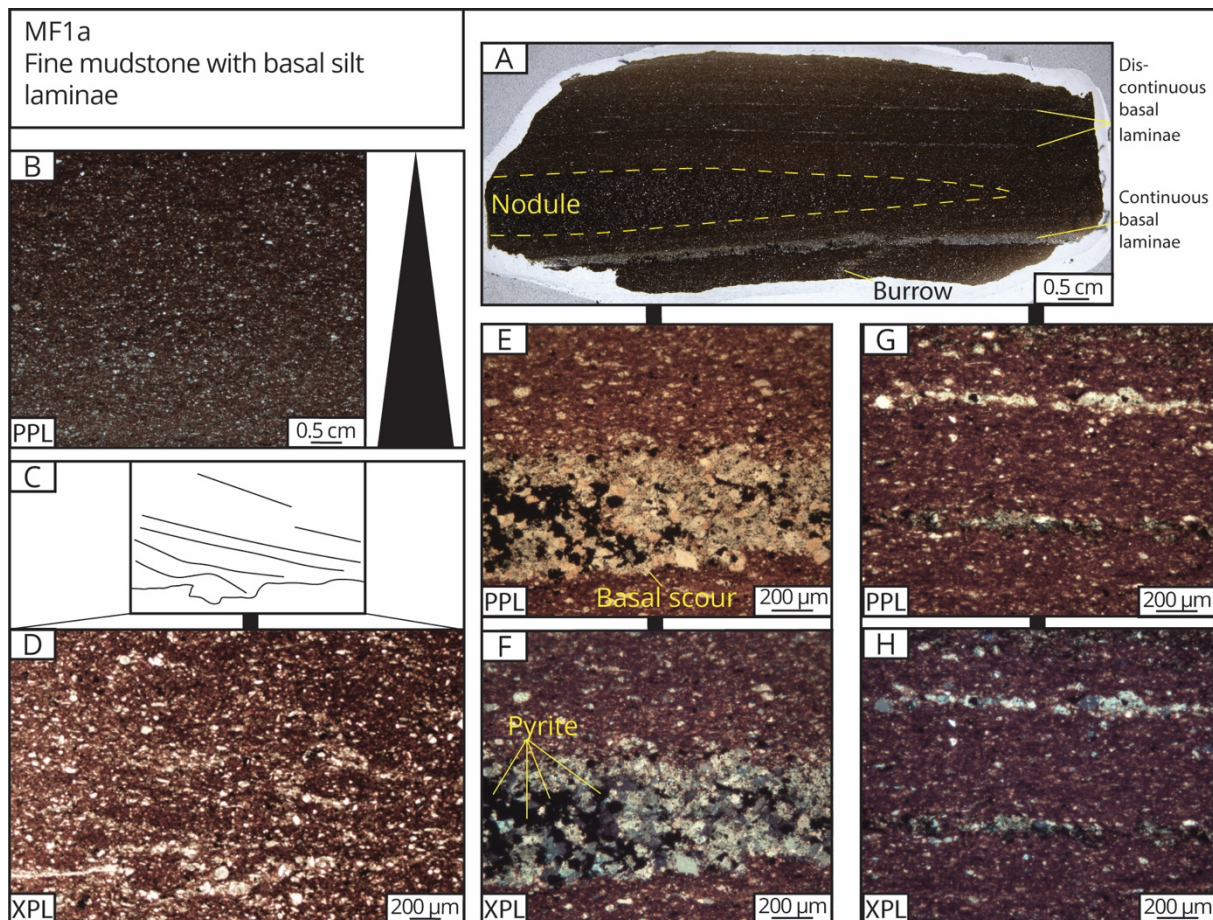
Figure 11: MF1a - Fine mudstone with basal silt laminae, interpreted to represent fine-grained turbidity currents. This microfacies shows evidence for bedload transport and waning currents. (A) Thin section overview. (B) Normal grading in the fine mud. (C–D) Laterally discontinuous set of cross-laminae that downlap asymptotically onto a basal scour. (E– F) Micrograph of continuous basal laminae, which are well-cemented and bear pyrite grains. (G–H) Micrograph of discontinuous basal laminae, which are a few grains thick and lenticular, pinching out and reappearing at the scale of millimeters.

4.4 MF4: Calcisphere packstone

Beds of this microfacies (MF4; fig. 16) are the product of suspension settling of pelagic bioclasts. Calcisphere packstones in other records are often interpreted as deposits of blooms that produce pelagic event beds (e.g. Tew 2000; Wilkinson 2011; Omaña et al. 2014). In the depositional environment of the McCarthy Formation, blooms are also interpreted to have caused rapid, episodic deposition of calcispheres, which outpaced the muddy background sedimentation to form packstones. The interpretation of episodic blooms is

supported by the presence of *Phycosiphon* sp. (fig. 16), which is often associated with event deposits (e.g. Rodríguez-Tovar, Nagy, and Reolid 2014).

4.5 MF5: Spiculitic sandy mudstone

The relatively poorly sorted assemblage of broken bioclasts show that this microfacies is the product of reworking (MF5; fig. 17). This microfacies occurs in cherts and carbonate concretionary horizons. These lithologies have a similar spiculitic framework, but the concretions contain less mud and more sparite (fig. 17C, D). The compositional contrast between the cherts and concretions is therefore interpreted to be the result of winnowing, which removed the siliceous fine mud from the beds in which carbonate concretions would grow during early diagenesis.

4.6 MF6: Laminated sandy mudstone

The medium to thick beds of MF6a show bigradational sorting – reverse to normal grading within the same bed (fig. 10C) – and are therefore interpreted to represent contour current deposits. Bigradational sorting is diagnostic for contour currents (e.g. Stow and Faugères 2008; Rebesco et al. 2014; Rodríguez-Tovar et al. 2019), but has also been associated with hyperpycnal flows caused by fluvial input (e.g. Shanmugam 2018). In the McCarthy Formation, there is no evidence for fluvial influence on the depositional environment, so a contouritic origin is more likely. The basal fining-upward laminae and the small-scale cross-laminae in the lower part of beds (fig. 18D–
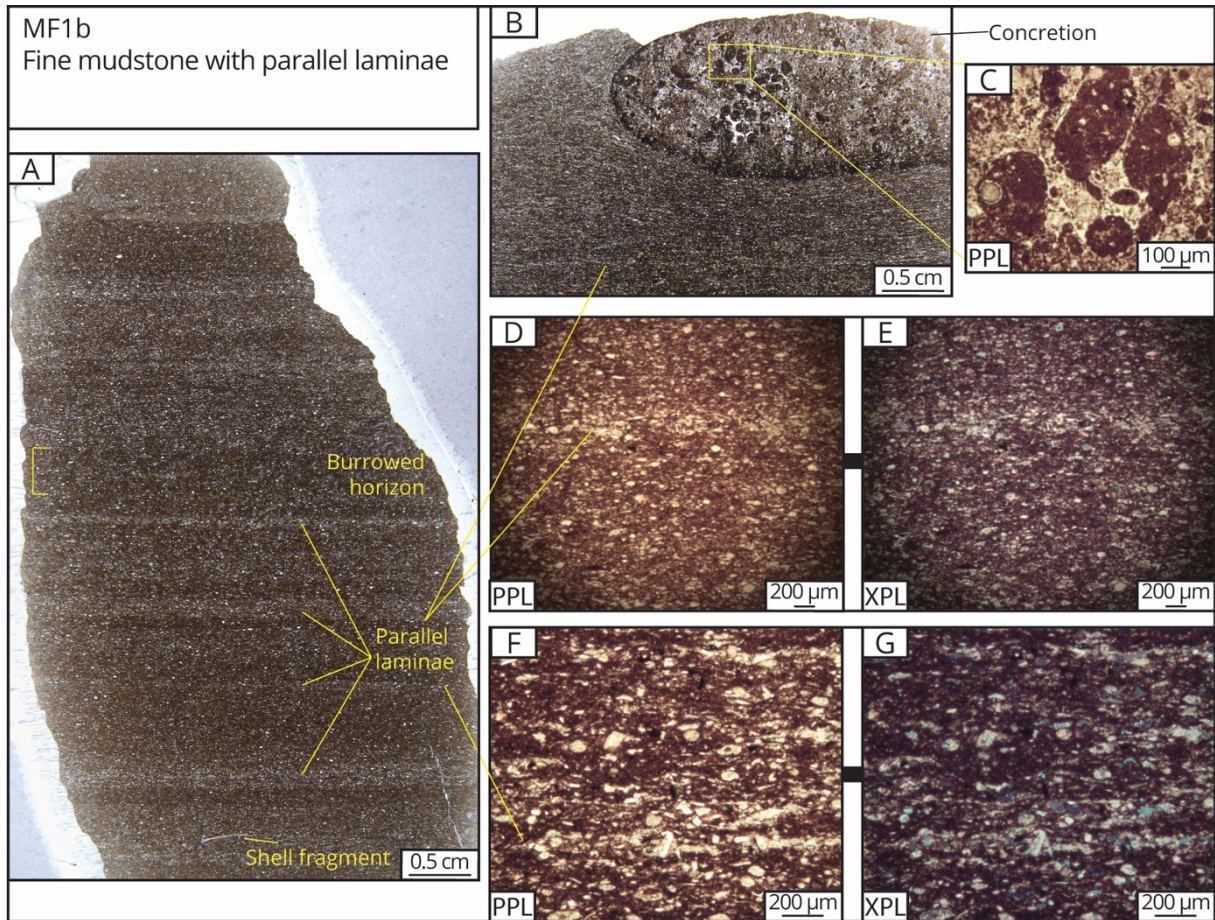
Figure 12: MF1b - Fine mudstone with parallel laminae, interpreted to represent suspension settling. (A) Thin section overview. (B–C) Concretion with an infill of sand-sized peloids, in which the primary texture of the fine mud is preserved. (D–G) Micrograph of laminae showing gradational contacts. The laminae are typically richer in cement than the surrounding fabric.

F) represent the waxing phase of the contour current, whereas the planar laminae in the coarsest interval represent the peak flow velocity (fig. 18A–C).

The wavy fabric that characterizes MF6b (fig. 18G) is interpreted to represent the colonization of microbial mats (see Schieber 2007). Given the setting of the McCarthy Formation below storm wave-base, the organic filaments that sometimes drape the wavy laminae are interpreted as the lamellar remnants of an aphotic microbial mat. Although this microfacies shows evidence for biological activity, most of the fabric consists of detrital
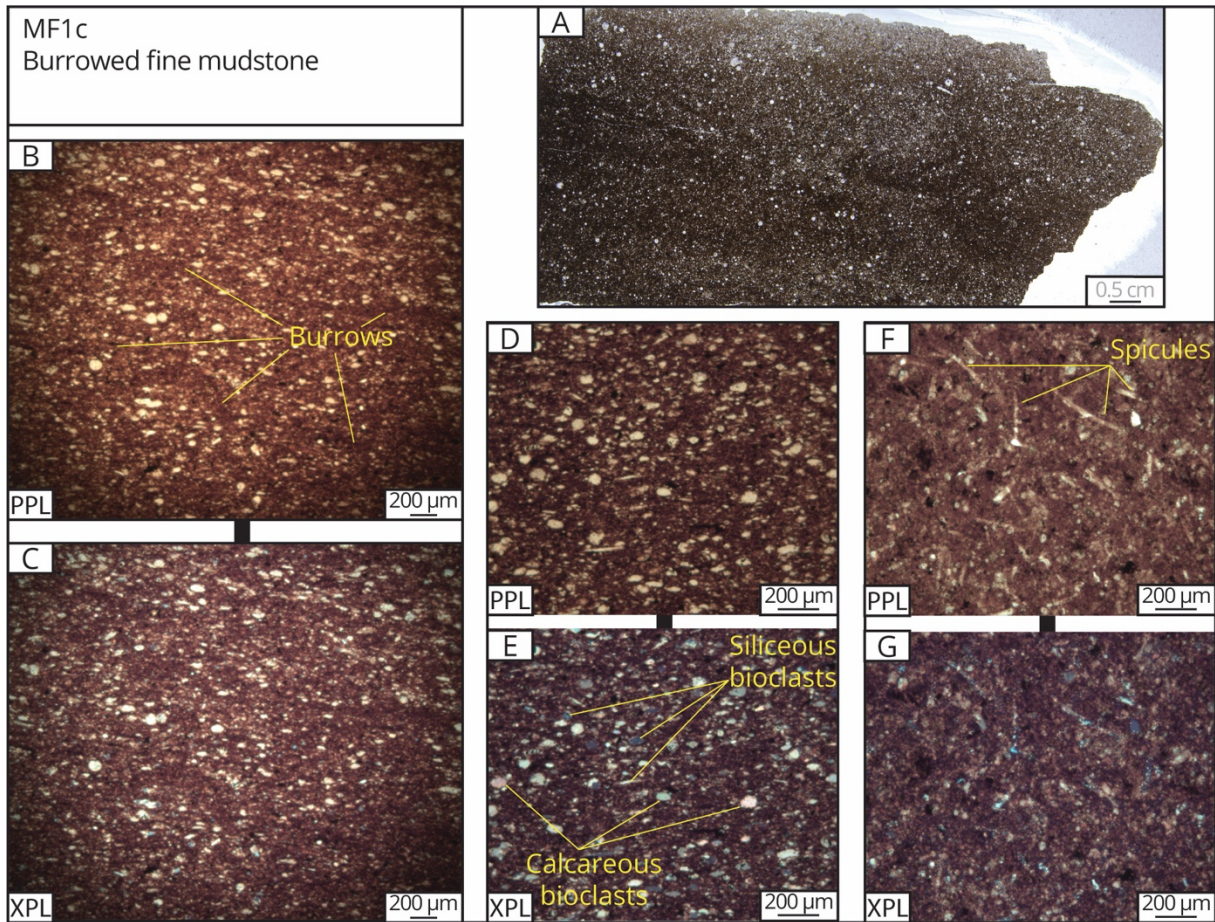
Figure 13: MF1c - Burrowed fine mudstone. Some beds of this microfacies represents background sedimentation, whereas others represent more dynamic processes (see section 4.1 for discussion). (A) Thin section overview. (B–C) Micrograph with recognizable burrows, which shows that the fabric has not completely been homogenized by bioturbation. Some of the burrows are *Phycosiphon* sp. (D–E) Many fine mudstones contain both siliceous microfossils, like radiolarians, and calcareous microfossils, like calcispheres. (F–G) An anomalous sample from the lower member (FA1) bearing reworked spicules, which are a subordinate bioclast in the lower member.

grains, which, based on the association with MF6a, were probably deposited

by bottom currents before they were colonized by microbial mats.
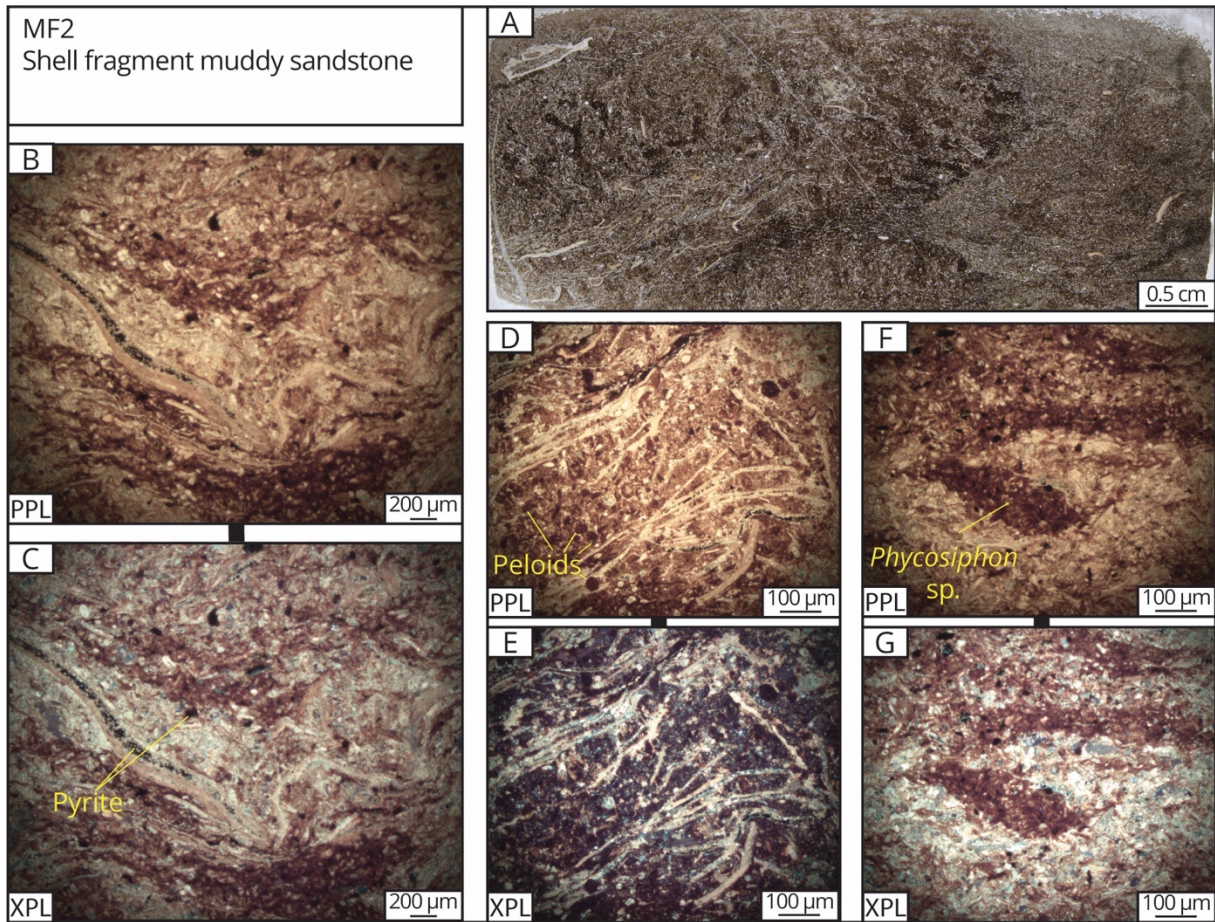
Figure 14: MF2 – Shell fragment muddy sandstone, interpreted to represent reworked deposits. (A) Thin section overview showing fine shell fragments in most of the fabric, with subordinate coarser shell fragments and mud-filled burrows. (B–C) The shell fragments are cemented together and sometimes filled with pyrite. (D–E) Sample that shows calcareous shell fragments in a siliceous matrix. (F–G) The characteristic fishhook-shape of *Phycosiphon* sp., which is often associated with event deposition (e.g. Rodríguez-Tovar, Nagy, and Reolid 2014).

5. Discussion

5.1 Paleogeography of the ramp

I constructed isopach maps for the Chitistone, Nizina, and McCarthy Formations (fig. 19; see also Appendix C). The orientation of the isopachs is approximately northwest-southeast (fig. 19) and probably reflects the depositional strike of the ramp. The thickness pattern of the three formations is consistent with a depositional dip towards the southwest: the Chitistone Formation, which represents the shallowest part of the ramp (Armstrong, MacKevett, and Silberling 1969), thickens toward the northeast, whereas the Nizina and the McCarthy Formations, which represent deeper environments, are thicker toward the southwest. Although this thickness pattern is consistent with observations made by Martin (1916), the interpretation of a depositional dip towards the southwest differs from Trop et al.'s (2002) suggestion that the ramp dipped towards the northeast.

The McCarthy Formation was deposited below storm wave-base, and its depositional environment may, thus, be referred to as an outer ramp (sensu Burchette and Wright 1992). We can infer that the outer ramp was a linear-sourced system (sensu Reading and Richards 1994): the reworked bioclasts of the McCarthy Formation were produced in the sediment factory (e.g. MF2, fig. 14; MF5, fig. 17), which follows the coastline and is therefore a linear sediment source. For this reason, the basin-scale architecture of the McCarthy Formation probably resembles those of linear-sourced siliciclastic slopes, where lobes of reworked sediment are deposited everywhere along
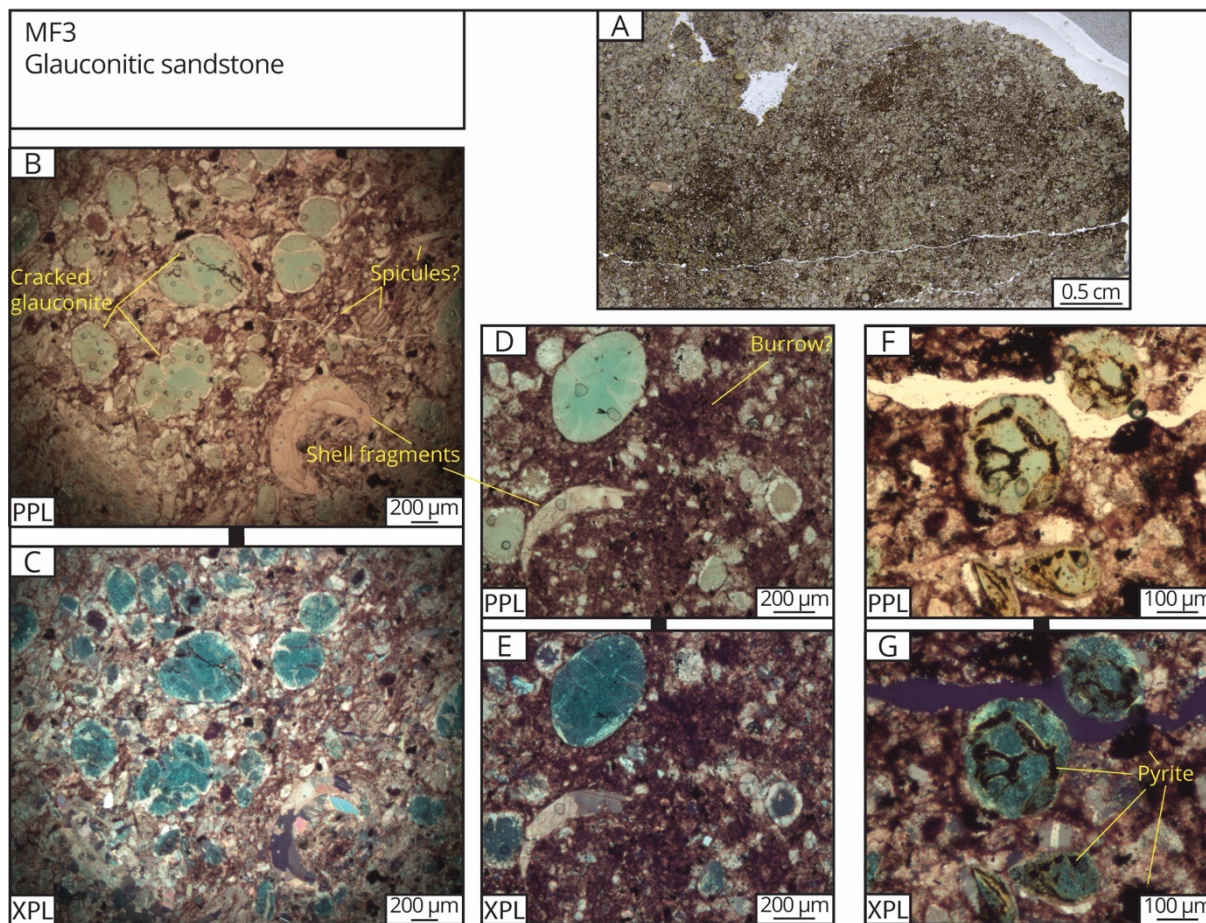
Figure 15: MF3 – Glauconitic muddy sandstone, interpreted to represent reworking followed by *in situ* glauconitization. (A) Thin section overview. (B–C) The glauconite is associated with reworked shell fragments and subordinate spicules. (D–E) The uniform, well-rounded glauconite grains are interpreted as glauconitized fecal pellets. (F–G) Some glauconite grains are glauconitized microfossils, evidenced by the foraminiferal internal structures of these grains.

depositional strike (e.g. Surlyk 1987). Alternatively, the McCarthy Formation can represent a multiple point-sourced system, if shallow-water sediment was funneled during transport to the outer ramp. A single-point source is unlikely, because the low Al% (fig. 3A) shows that lithogenic input from a river, which would have formed the single-point source, was insignificant during the deposition of the McCarthy Formation.

5.2 Sedimentology of the outer ramp

5.2.1. Sediment reworking to the outer ramp

In the McCarthy Formation, reworked sediment is concentrated stratigraphically in thick-bedded intervals (FA1, fig. 6; FA2, fig. 7), which are interpreted as lobe complexes (fig. 20). Although most reworked deposits of the McCarthy Formation are bioclastic (MF2, fig 14; MF5; fig. 17), the lobe complex of FA1 also contains fine mudstones that represent fine-grained turbidity currents (MF1a; fig. 11D). This finding in the record of a biogenic ramp is consistent with recent studies that show that biogenic mud is not only the product of constant background sedimentation, but can also be deposited by more dynamic processes (e.g. Schieber et al. 2013; Birgenheier and Moore 2018). The partings in FA1 (fig. 6) represent autogenic lobe abandonment, during which glauconitization took place (MF3; fig. 15), nodules formed (fig. 11A), concretions grew (fig. 7B), and hemipelagic mud was deposited. The lobe complexes of FA1 and FA2 illustrate the impact of reworking as a sediment delivery mechanism to the outer ramp, which is in line with previous studies that stress the role of reworking on ancient ramps (e.g. Puga-Bernabéu et al. 2014).

The alternation of the thick-bedded intervals (FA1 and FA2) and thin-bedded intervals (FA3 and FA4) of the McCarthy Formation represents a fluctuating sediment supply to the outer ramp. Whereas the thick-bedded intervals represent lobe-complexes, the thin-bedded facies intervals were deposited while supply of reworked sediment to the outer ramp was reduced and represent sediment-starved environments. This is evidenced by the
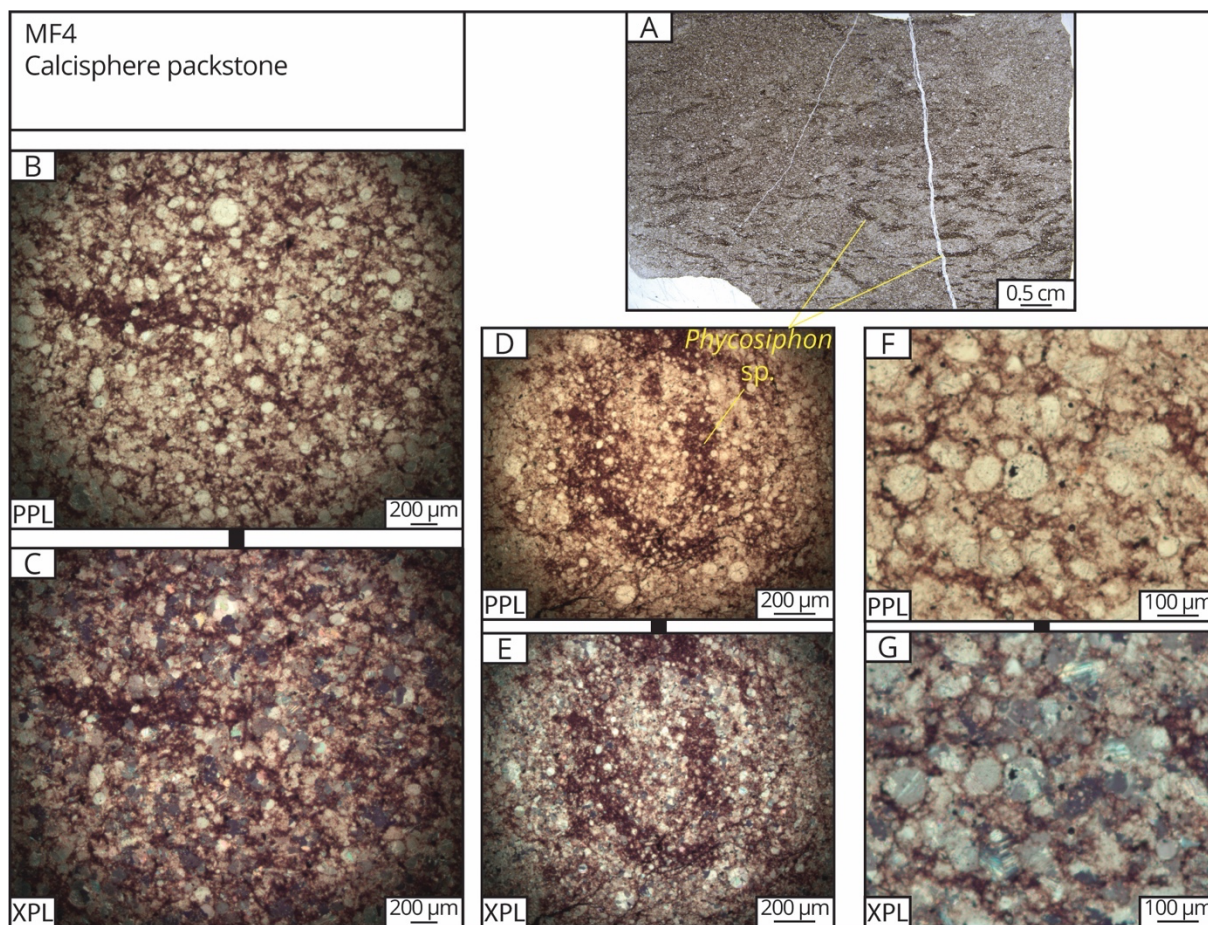
Figure 16: MF4 – Calcisphere packstone, interpreted to represent pelagic bloom deposits. (A) Thin section overview. The darker material represents mud-filled burrows. (B–G) Outside of the burrows, the fabric is rich in calcite cement. (D–E) *Phycosiphon* sp. is associated with event deposition (e.g. Rodríguez-Tovar, Nagy, and Reolid 2014), which supports the interpretation of episodic blooms.

scarcity of reworked bioclasts compared to the lobe complexes, the high burrowing-intensity (MF1c, fig. 13; MF4, fig. 14), and the low linear sedimentation rate of the Rhaetian (part of FA3) compared to the Hettangian (Table 3). The sediment-starved environments were dominated by background sedimentation, which is represented by burrowed fine mudstones (MF1c; fig. 13) and by calcisphere packstones, which reflect pelagic blooms (MF4; fig. 14). However, even though the supply of reworked shallow-water bioclasts was reduced, some fine mud was still delivered to the outer ramp by turbidity currents or debris flows (see section 4.1). This is consistent with

siliciclastic deepwater systems, where turbidity currents and debris flows also deliver mud to the basin-floor when the sand supply is reduced (Boulesteix et al. 2021).

The sediment-starvation of the depositional environment of FA3 is allogenic and probably represents biological distress and relative sea-level rise. The sediment starvation is interpreted to have an allogenic cause, because FA3 is latest Norian to earliest Hettangian in age (Caruthers et al. 2021), which shows that the sediment-starvation lasted at least ~8 Ma. As the Late Triassic had prolonged episodes of extinction (e.g. Lucas and Tanner 2018), sediment production rates on the ramp were likely reduced, which combined with ongoing post-volcanic subsidence (Trop et al. 2002) would have resulted in a long-term transgression and sediment-starvation on the outer ramp.

5.2.2. Bottom currents on the outer ramp

By comparing the lower member (FA1 and FA3) to the upper member (FA2 and FA4), we can infer that the member boundary reflects a change in the bottom current regime. In the Hettangian, bottom currents start impacting the deposition of the upper member. This is indicated by the bigradational beds of FA4 (fig. 10C), which are interpreted to represent contour currents (see section 4.6). Furthermore, the compositional contrast between the cherts and carbonate concretions of FA2 – which are both rich in siliceous spicules – is interpreted to have been produced by bottom currents: After the spiculitic sediment was reworked to the outer ramp, bottom currents formed dunes (fig.
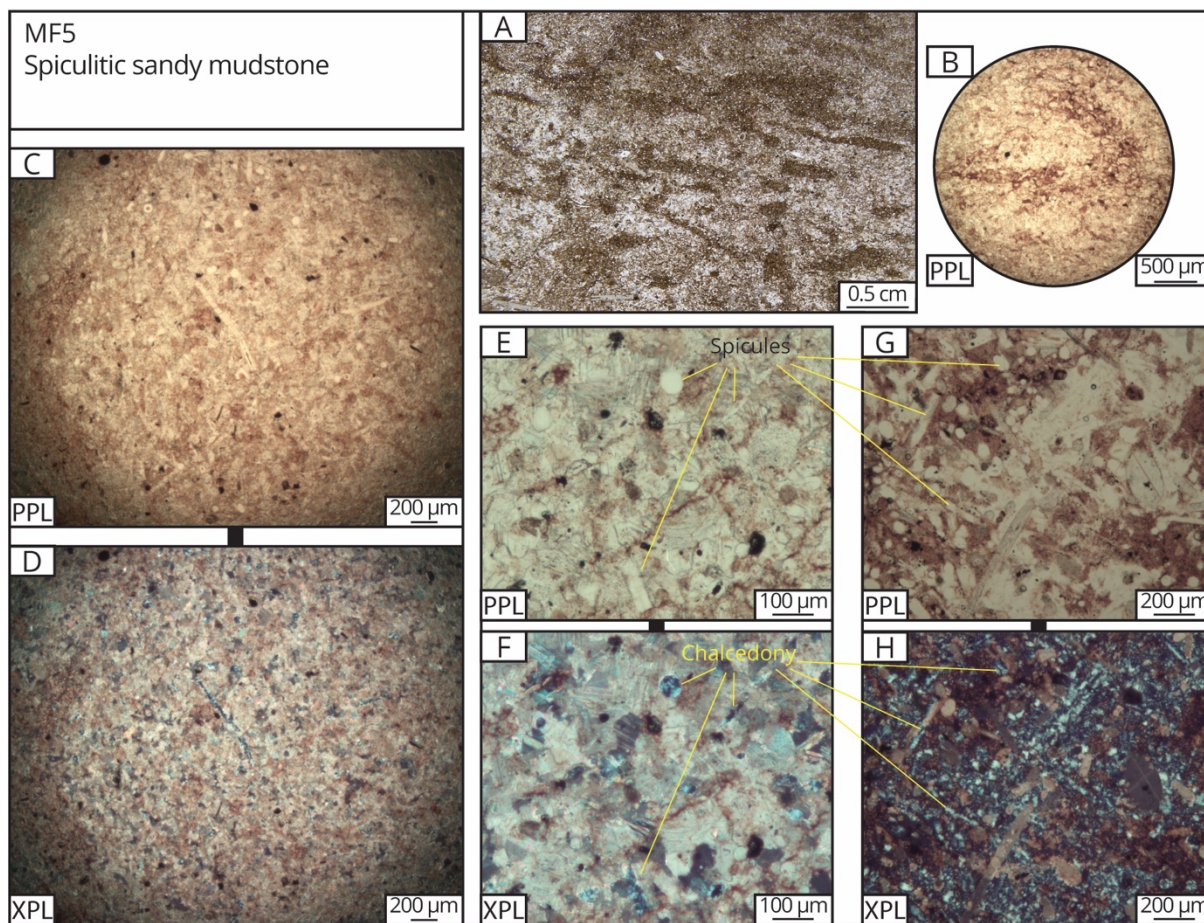
Figure 17: MF5 – Spiculitic sandy mudstone, interpreted to represent reworked deposits. This microfacies is present in the cherts and carbonate concretions of FA2. (A) Thin section overview of a spiculitic chert. (B) *Phycosiphon* sp., which is associated with punctuated deposition (e.g. Rodríguez-Tovar, Nagy, and Reolid 2014). (C–F) Concretions show siliceous spicules, which are filled with chalcedony, in sparry cement. (G–H) Spiculitic chert. The concretions and the cherts both contain spicules, but the concretions contain less mud and more sparite than the cherts. This is interpreted to represent winnowing by bottom currents of the beds in which concretions would eventually grow.

7D) and winnowed the siliceous mud from the strata in which concretions would eventually grow (fig. 17E). The beds that were not affected by bottom currents formed cherts (fig. 17G).

The sets of large scale cross-stratification in FA2 (fig. 8) are interpreted as a bottom current-induced sediment drift. Sets of large-scale cross-stratification in ramp records are often interpreted as progradational clinoforms on the slope of distally steepened ramps (e.g. Puga-Bernabéu et
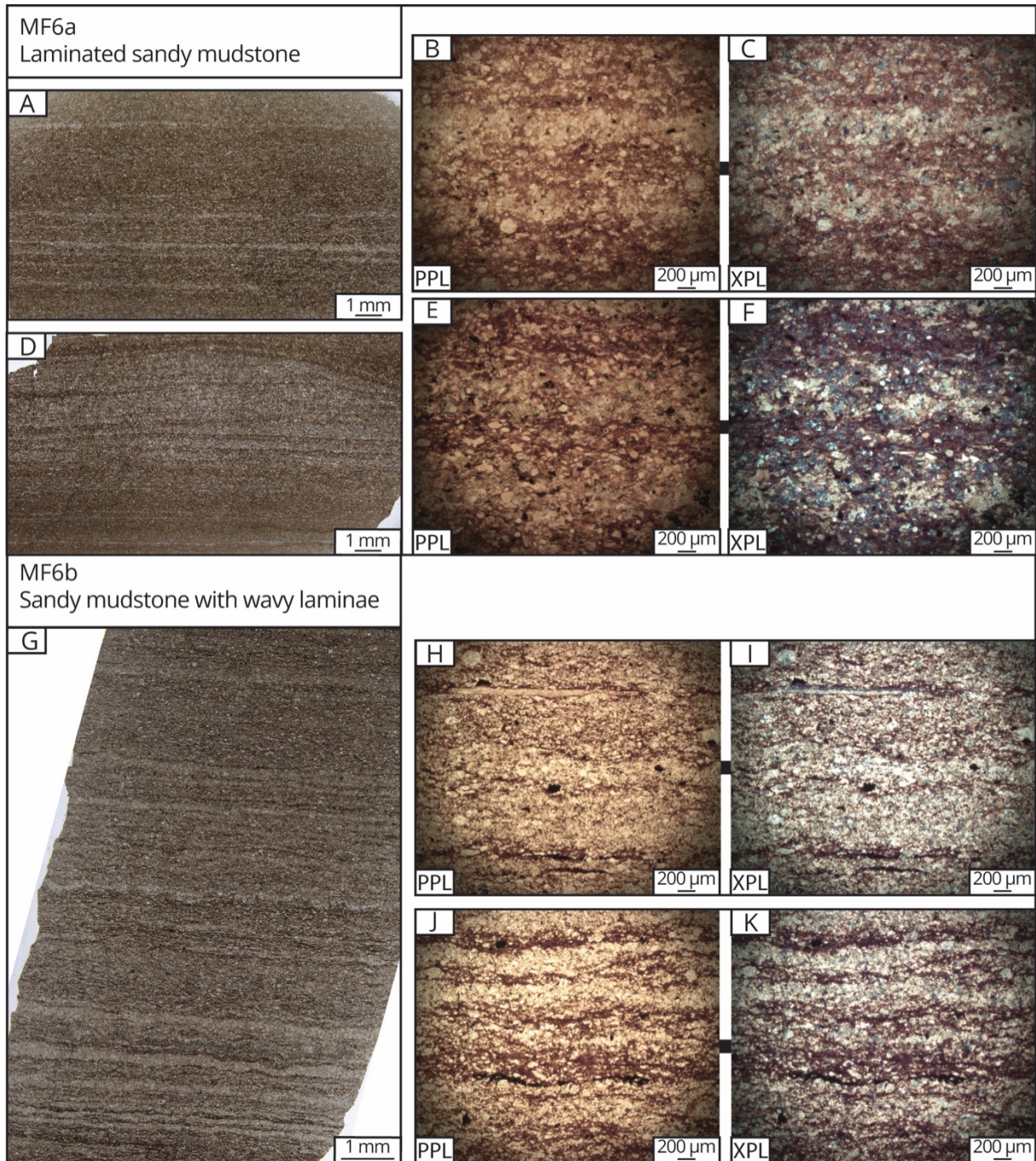
Figure 18: MF6 – Laminated sandy mudstone. (A–F) MF6a is characterized by the more planar laminae compared to MF6b and occurs in beds with bigradational sorting, which are interpreted as contourites. (A–C) In thin section, the coarsest middle part of such beds contains planar parallel laminae represents peak flow velocity. (D–F) The finer material at the base of the bigradational beds contains slightly more siliceous fine mud, as well as basal and cross-laminae. (G–K) MF6b is characterized by wavy laminae and represents a detrital deposit that was colonized by microbial mats. The laminae are sometimes draped by lamellar organic material (opaque).

al. 2010; Puga-Bernabéu et al. 2014), but compared to these examples, the sets of cross-stratification observed in this study are smaller and less steep. Instead, the sets cross-stratification of FA2 are interpreted as a sediment drift, based on other evidence in the upper member that can be linked to bottom currents: FA2 also contains channelforms (fig. 8), dune cross-stratification (fig. 7) and winnowed beds (fig. 17E), and is associated with the contouritic beds of FA4 (fig. 10C). FA2 thus represents an outcrop analogue for biogenic drift systems that have been observed in seismics (e.g. Reolid, Betzler, and Lüdmann 2019).

5.3 The Early Jurassic glass ramp of Wrangellia

The boundary between the lower and upper members of the McCarthy Formation marks a transition in the composition of reworked bioclasts from calcareous to siliceous. This shows that in the Hettangian, the depositional environment transitioned from a siliceous carbonate-ramp to a glass ramp (fig. 20).

The lower member of the McCarthy Formation represents a siliceous carbonate-ramp (fig. 20). Although many facies of the lower member are siliceous (fig. 3A), most of this silica is not present in reworked spicules, but in radiolarian tests, chert nodules, and microcrystalline phases (fig. 3B). Most reworked bioclasts in the lower member are calcareous shell fragments, which form packstones (MF2; fig. 14) and are incorporated in other lithologies (e.g. MF3; fig. 15). This shows that calcite-secreting biota
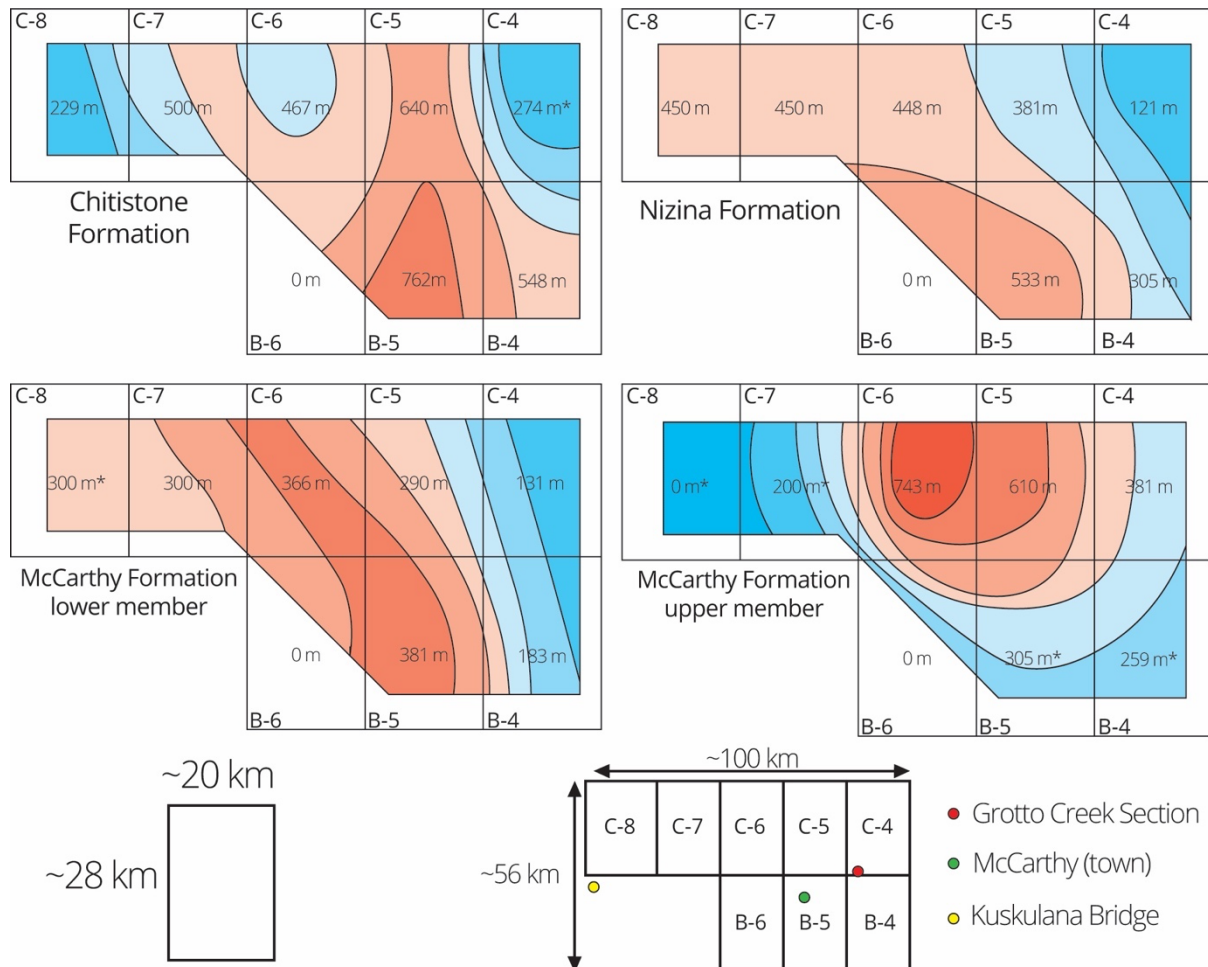
Figure 19: Isopach maps of the Late Triassic to Early Jurassic of the Wrangell Mountains, based on maximum thicknesses reported for each quadrangle (MacKevett 1970a; 1970b; 1972; 1974; 1978; MacKevett and Smith 1972a; 1972b; Winkler and MacKevett 1981). *Top or base not exposed. Isopachs are oriented NW-SE, which reflects the depositional strike. The depositional dip is interpreted to be towards the SW based on the thickness pattern: The Chitistone Formation, which represents the shallowest environments (Armstrong, MacKevett, and Silberling 1969), pinches towards the southeast, whereas the Nizina and McCarthy Formations, which represent more distal environments, pinch towards the northwest.

produced more sediment than siliceous sponges in the shallow-water sediment factory during the deposition of the lower member.

The glass ramp environment of the upper member (fig. 20) is reflected in the spiculitic microfacies (MF5; fig. 17), which resemble the transported spiculite facies of other Hettangian glass ramps (Ritterbush et al. 2014; 2015; Ritterbush, Ibarra, and Tackett 2016). The more siliceous nature of the upper member is also evidenced by bedded cherts, which appear exclusively in the
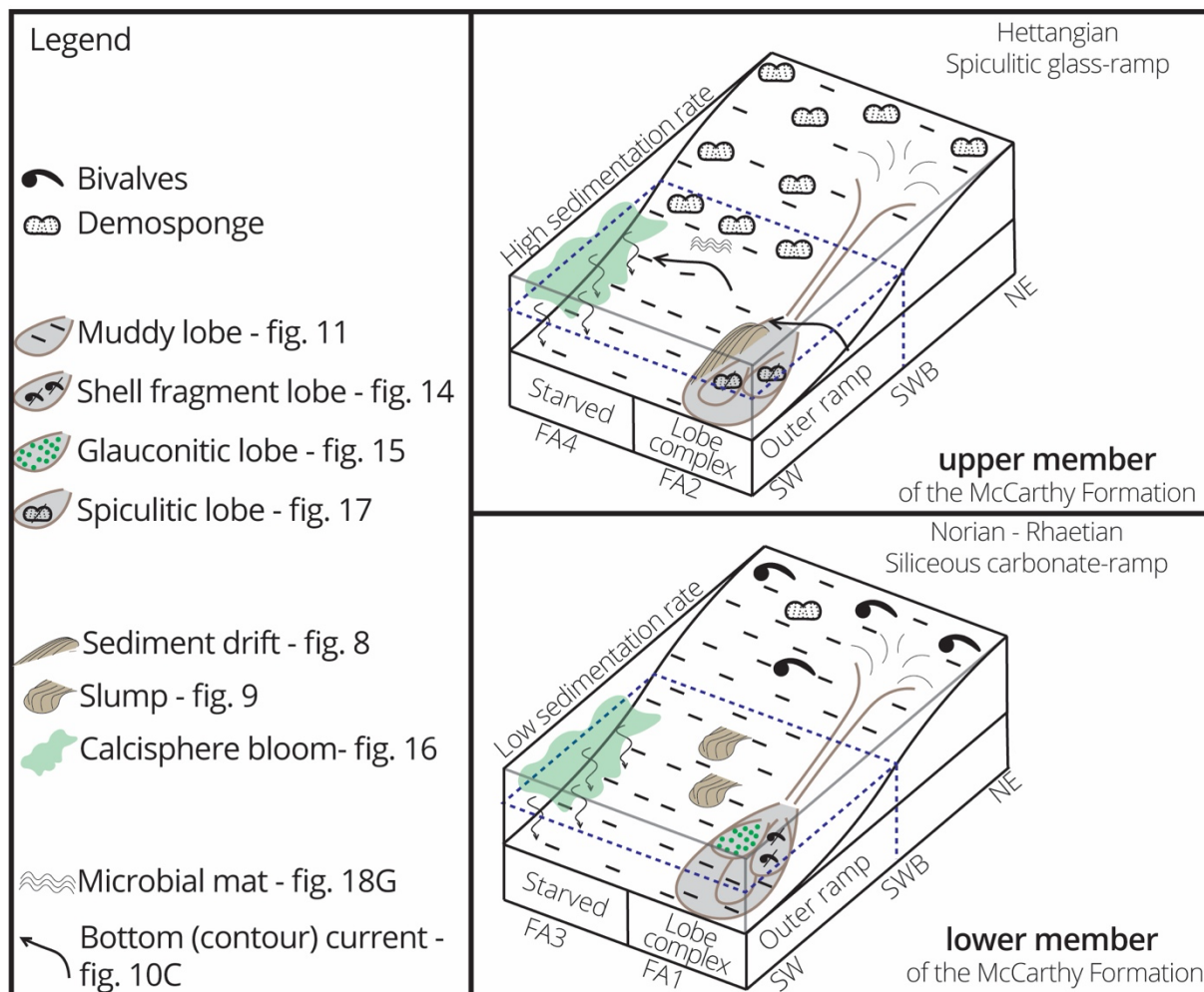
Figure 20: Schematic summary of the depositional environments of the McCarthy Formation. No scale intended. The McCarthy Formation represents an outer ramp with a fluctuating supply of reworked shallow-water sediment, marked by the alternation of lobe complexes (FA1 and FA2) and sediment-starved environments (FA3 and FA4). During the deposition of the upper member, bottom currents affected deposition on the outer ramp. The reworked bioclasts are more siliceous in the upper member, which marks a transition from a siliceous carbonate-ramp to a spiculitic glass ramp in the Hettangian. This transition coincides with an order of magnitude increase in sedimentation rates, which illustrates how increased shallow-water sediment production can increase the sediment supply to the outer ramp.

upper member (fig. 3A), and by the quartz/calcite XRD intensity ratios, which are generally higher in the upper member than in the lower member (fig. 4). Although the upper member also contains calcareous lithologies, most are concretions that, like most cherts, also contain spicules (fig. 17E). The upper member therefore represents outer ramp environments with a spiculitic sediment supply on a glass ramp.

The transition from a siliceous carbonate-ramp to a glass ramp recorded in the McCarthy Formation shows that the biogeochemical regime that favored biosiliceous sedimentation was widespread in the Hettangian. The transition observed in this study is consistent with coeval records from the continental margins of Pangea (Delecat, Arp, and Reitner 2011; Ritterbush et al. 2014; 2015; Ritterbush, Ibarra, and Tackett 2016). The presence of a glass ramp on Wrangellia, an isolated terrane in the Panthalassan Ocean (Jones, Silberling, and Hillhouse 1977; Trop et al. 2002), supports the hypothesis that the weathering of the CAMP caused a global increase in oceanic silica concentrations, which promoted biosiliceous sedimentation and resulted in widespread glass ramps in the Early Jurassic (Ritterbush et al. 2015).

The silica supply from local Wrangellian basalts was probably minor compared to the silica supply from the CAMP. The low Al% shows that total lithogenic sediment supply to the ramp was low (fig. 3A), which is consistent with Trop's (2002) interpretation that there was "a general lack of high-relief, basin-bounding source terranes and volcanism" when the McCarthy Formation was deposited. Thus, local basalts may have formed a local silica source, but it probably had a minor effect on biogenic sediment production compared to the CAMP.

The transition from a siliceous carbonate-ramp to a glass ramp in the Hettangian coincided with an order of magnitude increase in the linear sedimentation rates from the Rhaetian to the Hettangian (table 3). The low linear sedimentation rate of the Rhaetian represents reduced sediment production during the end-Triassic mass extinction, whereas the higher

sedimentation rate of the Hettangian represents the reactivation of the outer ramp lobe complex as a result of increased sediment production during a recovery of silica-secreting biota. This contrast illustrates the role of sediment production in the shallows in controlling the rate and the composition of the sediment supply to the outer ramp.

6. Conclusions

The McCarthy Formation offers an insight into the sedimentology of outer ramps and biosiliceous sedimentation on Wrangellia from the Late Triassic to the Early Jurassic.

- The Late Triassic to Early Jurassic depositional environments of the Wrangell Mountains basin had a depositional dip towards the southwest.

- In both members of the McCarthy Formation, reworked sediment is concentrated in stratigraphic intervals that are interpreted as outer ramp lobe complexes. The stratigraphy outside of lobe complexes represents sediment-starved outer ramp environments where background sedimentation was more important. The alternation between these environments represent allogenic fluctuations in the bioclastic sediment supply to the outer ramp.

- The member boundary represents a change in the current regime, as bottom currents only affected the deposition of the upper member. Bottom currents formed a sediment drift on the outer ramp during the Hettangian.

- During the Norian and Rhaetian, the lower member was deposited in the outer ramp environments of a siliceous carbonate-ramp. From the Hettangian onwards, the upper member was deposited in the outer ramp environments of a spiculitic glass ramp. This finding represents a recovery phase of silica-secreting biota on Wrangellia following the end-Triassic mass extinction. This finding is consistent with coeval records from Pangea and supports the hypothesis that weathering of the Central

Atlantic Magmatic Province increased global oceanic silica concentrations (e.g. Ritterbush 2015; Ritterbush 2019).

- An order magnitude increase in sedimentation rates at Grotto Creek from Rhaetian to Hettangian coincided with the transition from siliceous carbonate-ramp to glass ramp. This shows how an increase in biogenic sediment production in shallow waters can impact the evolution of more distal environments – namely by increasing the sediment supply to the outer ramp.

References

Armstrong, Augustus K., Edward Malcolm MacKevett, and N. J. Silberling. 1969. "The Chitistone and Nizina Limestones of Part of the Southern Wrangell Mountains, Alaska - A Preliminary Report Stressing Carbonate Petrography and Depositional Environments." *US Geological Survey Professional Paper*, D49–62.

Baccelle, Lucia, and Alfonso Bosellini. 1965. *Diagrammi per La Stima Visiva: Della Composizione Percentuale Nelle Rocce Sedimentarie.* Vol. 4. Università degli studi di Ferrara.

Birgenheier, Lauren P., and Shawn A. Moore. 2018. "Carbonate Mud Deposited below Storm Wave Base: A Critical Review." Edited by Lauren P. Birgenheier and Howard Harper. *The Sedimentary Record* 16 (4): 4–10. https://doi.org/10.2110/sedred.2018.4.4.

Boulesteix, Kévin, Miquel Poyatos-Moré, David M. Hodgson, Stephen S. Flint, and Kevin G. Taylor. 2021. "Fringe or Background: Characterizing Deep-Water Mudstones beyond the Basin-Floor Fan Sandstone Pinchout." *Journal of Sedimentary Research* 90 (12): 1678–1705. https://doi.org/10.2110/jsr.2020.048.

Burchette, T. P., and V. P. Wright. 1992. "Carbonate Ramp Depositional Systems." *Sedimentary Geology* 79 (1): 3–57. https://doi.org/10.1016/0037-0738(92)90003-A.

Campbell, Charles V. 1967. "Lamina, Laminaset, Bed and Bedset." *Sedimentology* 8 (1): 7–26. https://doi.org/10.1111/j.1365-3091.1967.tb01301.x.

Caruthers, A. H., S. M. Marroquín, D. R. Gröcke, M. Golding, M. Aberhan, T. R. Them II, J. P. Trabucho-Alexandre, Y. P. Veenma, J. D. Owens, C. A. McRoberts, R. M. Friedman, J. Trop, D. Szűcs, J. Pálfy, and B. C. Gill. 2021. "New Evidence for Long Duration Rhaetian Stage and Regional Differences in Carbon Cycle Perturbations at the Triassic-Jurassic Transition from a Panthalassan Succession (Wrangell Mountains, Alaska)." *unpublished.*

Delecat, Stefan, Gernot Arp, and Joachim Reitner. 2011. "Aftermath of the Triassic–Jurassic Boundary Crisis: Spiculite Formation on Drowned Triassic Steinplatte Reef-Slope by Communities of Hexactinellid Sponges (Northern Calcareous Alps, Austria)." In *Advances in Stromatolite Geobiology*, by Joachim Reitner, Nadia-Valérie Quéric, and Gernot Arp, 131:355–90. Lecture Notes in Earth Sciences. Berlin, Heidelberg: Springer Berlin Heidelberg. https://doi.org/10.1007/978-3-642-10415-2_23.

Droser, M. L., and D. J. Bottjer. 1986. "A Semiquantitative Field Classification of Ichnofabric." *Journal of Sedimentary Research (1986)* 56 (4): 558-559. https://doi.org/10.1306/212F89C2-2B24-11D7-8648000102C1865D.

Dunham, Robert J. 1962. "Classification of Carbonate Rocks According to Depositional Textures" 38: 108–21.

Gates, Laura M., Noel P. James, and Benoit Beauchamp. 2004. "A Glass Ramp: Shallow-Water Permian Spiculitic Chert Sedimentation, Sverdrup Basin, Arctic Canada." *Sedimentary Geology* 168 (1): 125–47. https://doi.org/10.1016/j.sedgeo.2004.03.008.

Heinhuis, Youp. 2020. "Architecture of a Carbonate Ramp, Used to Infer its Depositional History." Bachelor's thesis, Utrecht University.

Jones, David L., and Benita Murchey. 1986. "Geologic Significance of Paleozoic and Mesozoic Radiolarian Chert." *Annual Review of Earth and Planetary Sciences* 14 (1): 455–92. https://doi.org/10.1146/annurev.ea.14.050186.002323.

Jones, David L., N. J. Silberling, and John Hillhouse. 1977. "Wrangellia—A Displaced Terrane in Northwestern North America." *Canadian Journal of Earth Sciences* 14 (11): 2565–77. https://doi.org/10.1139/e77-222.

Lazar, O. Remus, Kevin M. Bohacs, Joe H. S. Macquaker, Juergen Schieber, and Timothy M. Demko. 2015. "Capturing Key Attributes of Fine-Grained Sedimentary Rocks in Outcrops, Cores, and Thin Sections: Nomenclature and Description Guidelines" *Journal of Sedimentary Research* 85 (3): 230–46. https://doi.org/10.2110/jsr.2015.11.

Lucas, Spencer G., and Lawrence H. Tanner. 2018. "The Missing Mass Extinction at the Triassic-Jurassic Boundary." In *The Late Triassic World: Earth in a Time of Transition*, edited by Lawrence H. Tanner, 721–85. Topics in Geobiology. Cham: Springer International Publishing. https://doi.org/10.1007/978-3-319-68009-5_15.

MacKevett Jr., E.M. 1963. "Preliminary Geologic Map of the McCarthy C-5 Quadrangle, Alaska." Report 406. IMAP. USGS Publications Warehouse. https://doi.org/10.3133/i406.

———. 1970a. "Geologic Map of the McCarthy C-4 Quadrangle, Alaska." Report 844. Geologic Quadrangle. USGS Publications Warehouse. https://doi.org/10.3133/gq844.

———. 1970b. "Geologic Map of the McCarthy C-5 Quadrangle, Alaska." Report 899. Geologic Quadrangle. USGS Publications Warehouse. https://doi.org/10.3133/gq899.

———. 1972. "Geologic Map of the McCarthy C-6 Quadrangle, Alaska." Report 979. Geologic Quadrangle. USGS Publications Warehouse. https://doi.org/10.3133/gq979.

———. 1974. "Geologic Map of the McCarthy B-5 Quadrangle, Alaska." Report 1146. Geologic Quadrangle. USGS Publications Warehouse. https://doi.org/10.3133/gq1146.

———. 1978. "Geologic Map of the McCarthy Quadrangle, Alaska." Report 1032. IMAP. USGS Publications Warehouse. https://doi.org/10.3133/i1032.

MacKevett Jr., E.M., and James G. Smith. 1972a. "Geologic Map of the McCarthy B-4 Quadrangle, Alaska." Report 943. Geologic Quadrangle. USGS Publications Warehouse. https://doi.org/10.3133/gq943.

———. 1972b. "Geologic Map of the McCarthy B-6 Quadrangle, Alaska." Report 1035. Geologic Quadrangle. USGS Publications Warehouse. https://doi.org/10.3133/gq1035.

MacKevett Jr., E.M., James G. Smith, D. L. Jones, and G. R. Winkler. 1978. "Geologic Map of the McCarthy C-8 Quadrangle, Alaska." Report 1418. Geologic Quadrangle. USGS Publications Warehouse. https://doi.org/10.3133/gq1418.

Macquaker, J. H.S., and A.E. Adams. 2003. "Maximizing Information from Fine-Grained Sedimentary Rocks: An Inclusive Nomenclature for Mudstones." *Journal of Sedimentary Research* 73 (5): 735–44. https://doi.org/10.1306/012203730735.

Martin, George C. 1916. "Triassic Rocks of Alaska." *GSA Bulletin* 27 (1): 685–718. https://doi.org/10.1130/GSAB-27-685.

Moffit, Fred H., and Stephen R. Capps. 1911. "Geology and Mineral Resources of the Nizina District, Alaska." Washington: Government Printing Office.

Moffit, Fred Howard. 1930. *Notes on the Geology of Upper Nizina River*. US Government Printing Office.

———. 1938. *Geology of the Chitina Valley and Adjacent Area, Alaska*. U.S. Government Printing Office.

Omaña, Lourdes, José Ramón Torres, Rubén López Doncel, Gloria Alencáster, and Iriliana López Caballero. 2014. "A Pithonellid Bloom in the Cenomanian-Turonian Boundary Interval from Cerritos in the Western Valles–San Luis Potosí Platform, Mexico: Paleoenvironmental Significance" 31 (1): 18.

Payros, Aitor, Victoriano Pujalte, Josep Tosquella, and Xabier Orue-Etxebarria. 2010. "The Eocene Storm-Dominated Foralgal Ramp of the Western Pyrenees (Urbasa–Andia Formation): An Analogue of Future Shallow-Marine Carbonate Systems?" *Sedimentary Geology* 228 (3): 184–204. https://doi.org/10.1016/j.sedgeo.2010.04.010.

Pomar, Luis, José Miguel Molina, Pedro A. Ruiz-Ortiz, and Juan Antonio Vera. 2019. "Storms in the Deep: Tempestite- and Beach-like Deposits in Pelagic Sequences (Jurassic, Subbetic, South of Spain)." *Marine and Petroleum Geology* 107 (September): 365–81. https://doi.org/10.1016/j.marpetgeo.2019.05.029.

Puga-Bernabéu, Ángel, José M. Martín, Juan C. Braga, and Julio Aguirre. 2014. "Offshore Remobilization Processes and Deposits in Low-Energy Temperate-Water Carbonate-Ramp Systems: Examples from the Neogene Basins of the Betic Cordillera (SE Spain)." *Sedimentary*

Geology 304 (May): 11–27. https://doi.org/10.1016/j.sedgeo.2014.02.001.

Puga-Bernabéu, Ángel, José M. Martín, Juan C. Braga, and Isabel M. Sánchez-Almazo. 2010. "Downslope-Migrating Sandwaves and Platform-Margin Clinoforms in a Current-Dominated, Distally Steepened Temperate-Carbonate Ramp (Guadix Basin, Southern Spain)." *Sedimentology* 57 (2): 293–311. https://doi.org/10.1111/j.1365-3091.2009.01079.x.

Reading, Harold G., and Marcus Richards. 1994. "Turbidite Systems in Deep-Water Basin Margins Classified by Grain Size and Feeder System." *AAPG Bulletin* 78. https://doi.org/10.1306/A25FE3BF-171B-11D7-8645000102C1865D.

Rebesco, Michele, F. Javier Hernández-Molina, David Van Rooij, and Anna Wåhlin. 2014. "Contourites and Associated Sediments Controlled by Deep-Water Circulation Processes: State-of-the-Art and Future Considerations." *Marine Geology*, 50th Anniversary Special Issue, 352 (June): 111–54. https://doi.org/10.1016/j.margeo.2014.03.011.

Reolid, Jesús, Christian Betzler, and Thomas Lüdmann. 2019. "Facies and Sedimentology of a Carbonate Delta Drift (Miocene, Maldives)." *Sedimentology* 66 (4): 1243–65. https://doi.org/10.1111/sed.12575.

Ritterbush, Kathleen. 2019. "Sponge Meadows and Glass Ramps: State Shifts and Regime Change." *Palaeogeography, Palaeoclimatology, Palaeoecology* 513 (January): 116–31. https://doi.org/10.1016/j.palaeo.2018.08.009.

Ritterbush, Kathleen A., David J. Bottjer, Frank A. Corsetti, and Silvia Rosas. 2014. "New Evidence on the Role of Siliceous Sponges in Ecology and Sedimentary Facies Development in Eastern Panthalassa Following the Triassic–Jurassic Mass Extinction." *PALAIOS* 29 (12): 652–68. https://doi.org/10.2110/palo.2013.121.

Ritterbush, Kathleen A., Yadira Ibarra, and Lydia S. Tackett. 2016. "Post-Extinction Biofacies of the First Carbonate Ramp of the Early Jurassic (Sinemurian) in NE Panthalassa (New York Canyon, Nevada, USA" *PALAIOS* 31 (4): 141–60. https://doi.org/10.2110/palo.2015.021.

Ritterbush, Kathleen A., Silvia Rosas, Frank A. Corsetti, David J. Bottjer, and A. Joshua West. 2015. "Andean Sponges Reveal Long-Term Benthic Ecosystem Shifts Following the End-Triassic Mass Extinction." *Palaeogeography, Palaeoclimatology, Palaeoecology* 420 (February): 193–209. https://doi.org/10.1016/j.palaeo.2014.12.002.

Rodríguez-Tovar, Francisco Javier, Francisco Javier Hernández-Molina, Heiko Hüneke, Estefanía Llave, and Dorrik Stow. 2019. "Contourite Facies Model: Improving Contourite Characterization Based on the Ichnological Analysis." *Sedimentary Geology* 384 (April): 60–69. https://doi.org/10.1016/j.sedgeo.2019.03.010.

Rodríguez-Tovar, Francisco Javier, Jenö Nagy, and Matías Reolid. 2014. "Palaeoenvironment of Eocene Prodelta in Spitsbergen Recorded by the Trace Fossil Phycosiphon Incertum." *Polar Research* 33 (1): 23786. https://doi.org/10.3402/polar.v33.23786.

Rohn, Oscar. 1900. *A Reconnaissance of the Chitina River and the Skolai Mountains, Alaska*. US Geological Survey.

Schäfer, Priska, and Jack A. Grant-Mackie. 1998. "Revised Systematics and Palaeobiogeography of Some Late Triassic Colonial Invertebrates from the Pacific Region." *Alcheringa: An Australasian Journal of Palaeontology* 22 (2): 87–122. https://doi.org/10.1080/03115519808619194.

Schieber, Juergen. 2007. "Microbial Mats on Muddy Substrates – Examples of Possible Sedimentary Features and Underlying Processes," 18.

———. 2016. "Experimental Testing of the Transport-Durability of Shale Lithics and Its Implications for Interpreting the Rock Record." *Sedimentary Geology* 331 (January): 162–69. https://doi.org/10.1016/j.sedgeo.2015.11.006.

Schieber, Juergen, and John B. Southard. 2009. "Bedload Transport of Mud by Floccule Ripples—Direct Observation of Ripple Migration Processes and Their Implications." *Geology* 37 (6): 483–86. https://doi.org/10.1130/G25319A.1.

Schieber, Juergen, John B. Southard, Patrick Kissling, Britt Rossman, and Robert Ginsburg. 2013. "Experimental Deposition of Carbonate Mud from Moving Suspensions: Importance of Flocculation and Implications for Modern and Ancient Carbonate Mud Deposition." *Journal of Sedimentary Research* 83 (11): 1026–32. https://doi.org/10.2110/jsr.2013.77.

Schieber, Juergen, John Southard, and Kevin Thaisen. 2007. "Accretion of Mudstone Beds from Migrating Floccule Ripples." *Science* 318 (5857): 1760–63.

Schlager, Wolfgang. 2005. *Carbonate Sedimentology and Sequence Stratigraphy*. SEPM Society for Sedimentary Geology.

Schrader, Frank Charles, and Arthur Coe Spencer. 1901. *The Geology and Mineral Resources of a Portion of the Copper River District, Alaska*. US Government Printing Office.

Shanmugam, G. 2018. "The Hyperpycnite Problem." *Journal of Palaeogeography* 7 (1): 6. https://doi.org/10.1186/s42501-018-0001-7.

Slootman, Arnoud, Matthieu J. B. Cartigny, Andrea Moscariello, Massimo Chiaradia, and Poppe L. de Boer. 2016. "Quantification of Tsunami-Induced Flows on a Mediterranean Carbonate Ramp Reveals Catastrophic Evolution." *Earth and Planetary Science Letters* 444 (June): 192–204. https://doi.org/10.1016/j.epsl.2016.03.052.

Stow, D. A. V., and J. -C. Faugères. 2008. "Chapter 13 Contourite Facies and the Facies Model." In *Developments in Sedimentology*, edited by M. Rebesco and A. Camerlenghi, 60:223–56. Contourites. Elsevier. https://doi.org/10.1016/S0070-4571(08)10013-9.

Sugisaki, Ryuichi, Koshi Yamamoto, and Mamoru Adachi. 1982. "Triassic Bedded Cherts in Central Japan Are Not Pelagic." *Nature* 298 (5875): 644–47. https://doi.org/10.1038/298644a0.

Surlyk, Finn. 1987. "Slope and Deep Shelf Gully Sandstones, Upper Jurassic, East Greenland." *AAPG Bulletin* 71. https://doi.org/10.1306/94886ECF-1704-11D7-8645000102C1865D.

Tew, Berry H. 2000. "Depositional Setting of the Arcola Limestone Member (Campanian) of the Mooreville Chalk, Eastern Gulf Coastal Plain" 50: 157–66.

Trop, Jeffrey M, Kenneth D Ridgway, JMG Glen, and JM O'Neill. 2007. "Mesozoic and Cenozoic Tectonic Growth of Southern Alaska: A Sedimentary Basin Perspective." *SPECIAL PAPERS-GEOLOGICAL SOCIETY OF AMERICA* 431: 55.

Trop, Jeffrey M., Kenneth D. Ridgway, Jeffrey D. Manuszak, and Paul Layer. 2002. "Mesozoic Sedimentary-Basin Development on the Allochthonous Wrangellia Composite Terrane, Wrangell Mountains Basin, Alaska: A Long-Term Record of Terrane Migration and Arc Construction." *GSA Bulletin* 114 (6): 693–717. https://doi.org/10.1130/0016-7606(2002)114<0693:MSBDOT>2.0.CO;2.

Wilkinson, Ian P. 2011. "Pithonellid Blooms in the Chalk of the Isle of Wight and Their Biostratigraphical Potential." *Proceedings of the Geologists' Association*, October. https://doi.org/10.1016/j.pgeola.2011.09.001.

Winkler, Gary R., and E.M. MacKevett Jr. 1981. "Geologic Map of the McCarthy C-7 Quadrangle, Alaska." Report 1533. Geologic Quadrangle. USGS Publications Warehouse. https://doi.org/10.3133/gq1533.

Witmer, John W. 2007. "Sedimentology and Stratigraphy of the Upper Triassic - Lower Jurassic McCarthy Formation, Wrangell-St. Elias Mountains, South-Central Alaska." Bachelor's thesis, Bucknell University.

Yawar, Zalmai, and Juergen Schieber. 2017. "On the Origin of Silt Laminae in Laminated Shales." *Sedimentary Geology* 360 (October): 22–34. https://doi.org/10.1016/j.sedgeo.2017.09.001.

Appendix A: Extended microfacies descriptions

MF1: Fine mudstone

Dunham: Mudstone/Wackestone; N = 20;

Occurs in lower member and upper member; Part of FA1, FA3, FA4

This facies is defined by the large contribution of fine mud (~70-95%) that consists of micrite and microcrystalline quartz. The relative contribution of coarse mud and sand is variable, but together always make up less than 30% of the fabric. The grains of the coarse mud fraction are typically sub-angular and, if bioclastic, they lack internal structure. The sand fraction consist of very fine to medium sand-sized bioclasts, most of which are sub-angular spheres of chalcedony or calcite (fig. 13D, E). Some bioclasts are recognizable as radiolarians, calcispheres, or foraminifera. This microfacies is richer in chalcedony and siliceous bioclasts in the upper member than in the lower member. Three different samples contain nodules and carbonate concretions that are rich in sand-sized peloids (fig. 11A, fig. 12B). The nodules and concretions have sharp boundaries with the surrounding fabric.

In the field, this microfacies occurs in a broad range of facies. It forms medium grey to black siliceous mudstones and calcareous cherts, some of which are fissile and thin bedded, whereas others are medium to thick bedded. Beds of this microfacies are sometimes laminated (fig. 6D). In FA1, this microfacies often contains chert and apatite nodules with a diameter of ~4 cm.

MF1 may be further subdivided based on sedimentary structures and the intensity of bioturbation into fine mudstone with basal silt laminae (MF1a), with parallel laminae (MF1b), and burrowed fine mudstone (MF1c).

- MF1a: Fine mudstone with basal silt laminae

Dunham: Mudstone/Wackestone; N = 6; fig. 11

Occurs in both members; Common in FA1; Subordinate in FA2 and FA3

This microfacies is characterized by very thin basal laminae (fig. 11A). The basal contacts of these laminae are sharp and irregular, and produce scours of up to ~250 μm deep (fig. 11A, G). The grains within these laminae consist predominantly of calcite and pyrite, and the laminae are rich in siliceous or calcareous cements (fig. 11F, H). The thinnest basal laminae are a few grains thick and lenticular (fig. 11A, G), pinching out and reappearing at the scale of millimeters, whereas the thicker basal laminae are more continuous (fig. 11A). The upper contacts of the laminae seem to transition gradually to the overlying fine mud, although the contacts can appear to be sharp as a result of a higher intensity of cementation within the laminae compared to the fine mud (fig. 11E, F). The fine mud in between laminae sometimes shows grading (fig. 11B). One thin lamina is overlain by a set of downlapping asymptotic cross-laminae (fig. 11C, D). This set is laterally discontinuous and has a maximum thickness of approximately 1 mm. The bioturbation index is 2. Some burrows can be recognized, but the bedding is mostly undisturbed (fig. 11A).

- MF1b: Fine mudstone with parallel laminae

Dunham: Mudstone/Wackestone; N = 3; fig. 12

Occurs in lower member; Common in FA3; Subordinate in FA1

This facies is characterized by very thin to thin parallel laminae that have a thickness of up to ~1 cm (fig. 12A). The laminae lack sharp contacts, basal scours, and internal structures (fig. 12). The bioturbation index is 2; some burrows can be recognized in specific intervals, but the bedding is mostly undisturbed (fig. 12A).

- MF1c: Burrowed fine mudstone

Dunham: Mudstone/Wackestone; N = 11; fig. 12

Occurs in both members; Common in FA3 and FA4; Subordinate in FA1

This facies is characterized by a bioturbation index that ranges between 5 and 6 (fig. 12A). There are intervals with poorly defined, but still recognizable laminae, but the fabric has been mostly homogenized. Burrows have typical diameters of <1 mm. *Phycosiphon* sp., *Chondrites* sp., and *Planolites* sp. seem to be the dominant ichnospecies of the burrows that are still recognizable (fig. 12B, C).

MF2: Shell fragment muddy sandstone

Dunham: Packstone; N=2; fig. 14

Occurs in lower member; Occurs in FA3

This microfacies is characterized by large contribution (50-60%) of thin shell fragments (fig. 14A). The fabric also consists of coarse mud-sized calcite

grains and peloids, and fine mud. This microfacies bears bryozoans. Some shell fragments are filled with chalcedony, calcite, or pyrite (fig. 14C, E). The bioturbation index is 4, and recognizable ichnospecies are *Chondrites* and *Phycosiphon* (fig. 14A, F). In the field, this microfacies forms thin to thick, indurated beds of sandy limestone are interbedded with partings of black siliceous mudstone, which also contain abundant *Monotis*.

MF3: Glauconitic muddy sandstone

Dunham: Grainstone, Packstone, Wackestone; N=3; fig. 15

Occurs in lower member; Occurs in FA1;

This facies is characterized by a large contribution of well-rounded fine to medium sand grains that consist of glauconite. The glauconite grains frequently have calcite rims (fig. 15D), and cracks that are filled with calcite (fig. 15B) or framboidal pyrite (fig. 15G). Several glauconite grains show the pyritized internal structure of foraminifera (fig. 15F, G). This facies also contains shell fragments, and bears spicules and coarse mud to sand-sized grains of sub-angular calcite (fig. 15B, D). The bioturbation index is 5. In the field, this microfacies forms dark, medium to thick beds. One bed is a glauconitized packstone of *Heterastridium*.

MF4: Calcisphere packstone

Dunham: Packstone; N = 8; fig. 16

Occurs in lower member and upper member; Part of FA2, FA3, and FA4.

A structureless facies that is characterized by a large contribution of coarse mud and sand, that together make up 70-90% of the fabric. The samples of this microfacies fall in two fields of the Lazar et al. (2015) classification, and therefore, the name packstone is used. This coarser grain size fraction is dominated by calcispheres (fig. 16B). The term calcispheres is here used as a descriptive term for spherical, well-rounded grains of calcite (fig. 16G). The grains lack internal structure, making it difficult to differentiate biogenic precursors. Some samples contain a low amount of spicules (<5%). The rest of the fabric (10-30%) consists of fine mud. This microfacies contains burrows of the ichnospecies *Phycosiphon* sp. (fig. 16A, D, E), lacks sedimentary structures, and has a bioturbation index of 5. This microfacies is typically well-cemented and can form concretionary horizons.

In the field, this microfacies forms thin to thick beds of sandy limestone and calcareous chert. Beds of this microfacies are typically indurated, and have sharp contacts.

MF5: Spiculitic sandy mudstone

Dunham: Packstone; N = 6; fig. 17

Occurs in upper member; Occurs in FA2

This is a relatively coarse microfacies that is characterized by a large contribution of coarse mud and sand grains (>70%), that predominantly consists of bioclasts. The most common bioclasts are spicules (fig. 17E, G), that are often filled with chalcedony (fig. 17F, H). Subordinate bioclasts include echinoid fragments, radiolarians, calcispheres, and benthic

foraminifera. The fine mud (<30%) is mostly concentrated in muddier laminae, and in burrows (fig. 17A). This microfacies has a bioturbation index of 5, and sedimentary structures are therefore absent at the scale of a thin section (fig. 17A). *Phycosiphon* sp. can be recognized (fig. 17B).

In the field, this microfacies is present in concretionary horizons and in the cherts in between such horizons. In several concretionary horizons, we observed inclined surfaces that downlap asymptotically onto the underlying bedding plane (fig. 7D, E). The fabric of the chert samples is rich in chalcedony and siliceous mud. The concretionary samples have a similar contribution of spicules but contain less mud and more sparite. It should be noted that most bioclasts of the concretionary samples are also filled with chalcedony (fig. 17C, D).

MF6: Laminated sandy mudstone

Dunham: Packstone; N = 5; fig. 18

Occurs in upper member; Occurs in FA4

This microfacies is rich in coarse mud to sand-sized grains (>68%) that consist of calcite and subordinately of calcispheres and shell fragments (fig. 18). This microfacies is characterized by the fact that most of these coarser grains are concentrated in very thin laminae that tend to be well-cemented. In the field, this facies forms buff, laminated carbonate concretions with a height of ~25 cm (fig. 10C, D). This microfacies has a bioturbation index of 1. This microfacies can be subdivided further based on its sedimentary structures.

- MF6a: Laminated sandy mudstone with planar laminae

Dunham: Packstone; N = 2; fig. 18

Occurs in upper member; Part of FA4;

The ~25 cm thick beds of this microfacies show reverse grading followed by normal grading (fig. 10C). At this scale, the coarsest interval in the middle is a sandy mudstone (fig. 18A, B, C) that forms planar parallel laminae. The material above and below this coarse interval is a relatively fine chert that contains very thin beds with basal laminae that fine upwards, and sets of sigmoidal cross-laminae (fig. 18 D, E, F).

- MF6b: Laminated sandy mudstone with wavy laminae

Dunham: Packstone; N = 3; fig. 18

Occurs in upper member; Part of FA4

The beds of this microfacies are characterized by very thin wavy laminae (fig. 18G). The laminae represent an alternation of well-cemented calcite sand, and carbonaceous fine to coarse mud (fig. 18J). The wavy laminae have a wavelength of approximately 0.5 to 2 mm, and an amplitude of up to ~150 μm. This microfacies contains elongated organic filaments that tend to be oriented parallel to the bedding, and sometimes appear to drape the coarser laminae (fig. 18J, K).

Appendix B: Table of thin sections

Microfacies		Sample	Strat. Pos.	% Sand	% Coarse	% Fine
MF1	**MF1a**	B19	4.94	3	5	92
		B59	20.455	4	7	89
		B75	21.395	10	7	83
		B92	22.905	10	19	71
		GC46	71.905	14	10	75
		GC69	95.355	20	5	75
	MF1b	B12	4	5	15	80
		GC26.55	52.55	6	18	76
		GC56	81.505	10	14	76
	MF1c	B15	4.45	4	6	90
		GC2	28.305	16	9	75
		GC3	29.28	5	13	82
		GC18	44.365	8	15	78
		GC33.5	59.37	12	12	76
		GC36	62.02	15	13	72
		GC52	78.03	5	5	90
		GC58	83.5	12	8	80
		173.7	231.49	18	11	71
		174.5	232.29	10	10	80
		218.6	276.39	6	4	90
MF2		B24	5.745	60	14	26
		B30	8	50	20	30
MF3		B42-1	11.40	60	17	23
		B42-2*	11.68	71	19	10
		B46	16.73	35	21	44
MF4		B88*	22.71	35	40	25
		B112	25.43	40	42	18
		GC7	33.495	37	33	30
		GC20	46.365	33	41	26
		GC29	54.975	50	31	19
		GC41	66.905	55	27	18
		GC50*	75.505	44	38	18
		215.36*	273.15	60	29	11
MF5		32.28	90.07	45	35	20
		32.28B*	90.17	35	50	20
		32.62*	90.41	35	41	24
		124.76*	182.55	30	50	30
		124.86*	182.65	40	40	20
		131.2*	188.99	30	40	30
MF6	**MF6a**	209.05	266.84	30	49	21
		209.15	266.94	31	36	33
	MF6b	199.15	256.94	30	36	34
		199.75	257.54	37	29	38
		226.48	284.27	37	35	28

Appendix C: Fence diagram and basin infill
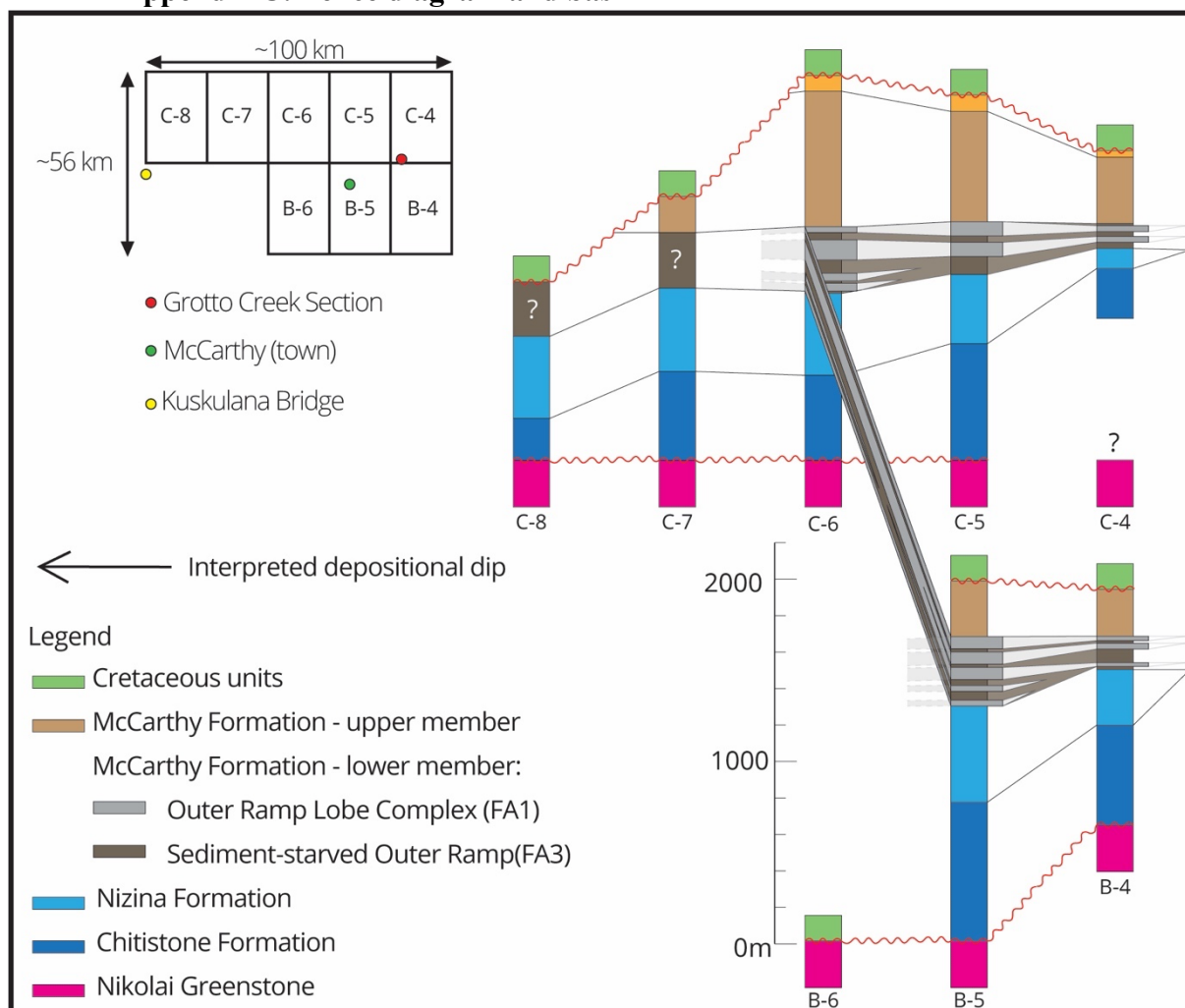
The figure above shows a fence diagram for the Late Triassic to Early Jurassic stratigraphy of the Wrangell Mountains basin, with additional detail for the lower member of the McCarthy, based on existing lithological columns (MacKevett 1970a; 1970b; 1972; 1974; 1978; MacKevett and Smith 1972a; 1972b; Winkler and MacKevett 1981). The C-7 and C-8 quadrangles have no lithological information. The correlation of the lower member is based on the assumption that the thick-bedded intervals and the thin-bedded bedded in the literature correspond to the thick-bedded and thin-bedded successions at Grotto Creek. The grey units of the lower member are thick-bedded

successions that, based on this study at Grotto Creek, are interpreted as outer ramp lobe complexes (FA1). The brown units of the lower member reflect sediment-starved outer ramp environments (FA3).

The main depocenter of the lower member is in the C-6 and B-5 quadrangles. Here, the lower member has a larger contribution of thick-bedded stratigraphy (viz. lobe complexes), whereas the more condensed stratigraphy in the C-4 and B-4 quadrangles has a larger contribution of hemipelagic sediment from sediment-starved environments. Based on this correlation and the inferred depositional dip towards the southwest, the Grotto Creek section was situated updip of the main depocenter.

The contacts between the formations are sharp in the east and laterally, toward the west, they become more gradual. These contacts are therefore interpreted to represent a gradual transgression, rather than a sudden basin-wide drowning. The contact between the Chitistone Formation and the Nizina Formation is sharp in the east (Green Butte, C-5 Quadrangle; Armstrong, MacKevett, and Silberling 1969), whereas in the west, the contact between these formations is gradational (C-7 Quadrangle; Winkler and MacKevett 1981). Likewise, the contact between the Nizina Formation and the McCarthy Formation is described as gradational in MacKevett (1978)'s general map of the full McCarthy Quadrangle, whereas locally, in the east, this contact is described as sharp (Green Butte; Armstrong, MacKevett, and Silberling 1969; Grotto Creek; Witmer 2007; fig. 1). The variability in the expressions of these contacts along the depositional dip, combined with the upward-deepening trend, therefore shows that the Late Triassic stratigraphy represents a gradual

transgression. This long-term transgression caused a landward migration of facies belts towards the northeast, resulting in a younging direction towards in the same direction.

The gradual transgression caused a diachronous infill of the basin. The preserved width of the formations in the Wrangell Mountains basin is approximately 100 km, even though the biogenic sediment factory of a homoclinal ramp with a dip of 0.1 degree (Burchette and Wright 1992) would have a width of only ~11 km. This means that the formations are diachronous and co-existed in different parts of the basin. Thus, when the Nizina Formation was still being deposited in the east, the McCarthy Formation was likely already being deposited in the west. The two lowermost grey units in the lower member of the McCarthy Formation at the C-6 and B-5 quadrangles, which don't correlate towards the east, are therefore probably the time-correlative of the Nizina Formation in the C-4 and B-4 quadrangles.

Appendix D: XRF data tables

Sample Name	Strat. Pos.	Al$_2$O$_3$	CaO	Fe$_2$O$_3$	K$_2$O	MgO	MnO	Na$_2$O	P$_2$O$_5$	SiO$_2$	TiO$_2$	Total
		%	%	%	%	%	%	%	%	%	%	%
σ* (%)	-	0.01	0.09	0.02	0.04	0.22	0.02	0.17	0.03	0.03	0.07	
B12	4	2.45	13.90	0.53	0.42	2.12	0.01	0.14	0.20	69.33	0.11	89.22
B19	4.94	3.79	12.71	0.93	0.75	1.81	0.01	0.35	0.05	69.44	0.24	90.09
B24	5.75	2.29	23.69	0.53	0.29	0.88	0.01	0.48	5.02	44.70	0.07	77.94
B30	8	3.40	22.98	1.00	0.55	1.67	0.01	0.45	0.10	48.70	0.12	78.98
B42	11.4	7.00	24.13	3.36	1.82	2.03	0.02	0.41	0.53	40.34	0.24	79.88
B59	20.46	3.50	16.03	2.10	0.57	1.05	0.03	0.52	1.62	62.77	0.22	88.40
B88	22.71	5.60	33.82	1.06	1.11	1.12	0.03	0.37	0.05	18.33	0.29	61.77
B92	22.91	6.39	14.40	2.31	1.03	1.48	0.02	0.99	0.09	61.22	0.38	88.31
GC 5	31.28	3.80	18.24	1.41	0.63	1.22	0.02	0.61	0.04	59.51	0.21	85.70
GC 9	35.28	3.68	21.79	1.50	0.70	1.29	0.03	0.53	0.07	51.64	0.22	81.47
GC 16	42.36	4.06	14.49	1.21	0.77	0.71	0.01	0.54	0.21	67.53	0.23	89.77
GC 22,45	48.45	3.40	17.46	1.38	0.51	0.62	0.01	0.62	0.08	61.73	0.19	86.00
GC 26	52	4.35	19.05	1.18	0.73	0.68	0.02	0.72	0.06	57.47	0.20	84.46
GC 26,55	52.55	3.52	13.96	1.23	0.58	0.57	0.02	0.64	0.12	68.75	0.20	89.58
GC 27	53	4.11	12.68	1.21	0.70	0.65	0.01	0.70	0.07	57.12	0.23	77.48
GC 28	53.75	5.44	10.32	1.84	0.89	0.81	0.02	0.90	0.13	71.29	0.28	91.91
GC 32,5	58.37	4.72	12.65	1.32	0.80	0.77	0.01	0.81	0.07	69.19	0.23	90.57
GC 37	63.02	5.73	17.12	1.60	1.17	0.77	0.02	0.64	0.07	59.73	0.28	87.12
GC 39	65.03	3.36	16.93	1.13	0.65	0.92	0.02	0.46	0.52	63.14	0.19	87.33
GC 42	68.03	2.68	20.63	0.91	0.50	0.62	0.02	0.47	0.06	57.64	0.15	83.67
GC 43	69.03	2.21	18.66	0.88	0.42	0.64	0.01	0.39	0.07	61.94	0.12	85.33
GC 49	75.03	3.08	33.94	0.62	0.63	0.78	0.06	0.25	1.42	16.38	0.08	57.23
GC 51	77.03	3.66	15.15	1.60	0.52	0.63	0.02	0.97	0.24	65.08	0.21	88.08
GC 61,5	87.53	3.22	18.28	1.27	0.48	0.60	0.02	0.83	0.08	60.18	0.20	85.16
GC 64	90.03	1.99	24.50	1.23	0.37	5.14	0.05	0.42	0.08	39.89	0.11	73.79
32,62	90.07	3.28	7.95	1.03	0.43	0.82	0.01	0.76	0.07	78.04	0.13	92.52
GC 66,5	92.53	6.10	16.95	1.70	1.18	0.71	0.02	0.92	0.04	58.30	0.22	86.14
GC 67,5	93.53	4.88	16.89	1.99	0.81	0.75	0.02	1.16	0.04	58.79	0.23	85.56
GC 70	96.03	2.01	20.40	0.81	0.41	0.65	0.02	0.34	0.05	58.39	0.11	83.19
124,86	182.65	6.88	11.01	0.66	1.33	0.52	0.01	1.02	0.05	68.89	0.13	90.50
174,15	232.29	5.84	4.84	2.73	0.67	0.85	0.04	1.94	0.15	76.54	0.42	94.02
199,75	257.54	9.16	2.65	3.19	1.60	1.32	0.02	1.32	0.06	73.66	0.36	93.33
215,36	273.15	3.89	28.95	1.69	0.35	0.62	0.31	1.78	0.03	26.96	0.28	64.85
218,60	276.4	5.53	7.30	1.16	1.00	0.57	0.03	1.37	0.54	76.64	0.19	94.33
226,48	284.27	3.58	23.90	1.07	0.67	0.70	0.18	1.00	0.09	45.84	0.22	77.23
ISE921	-	12.01	6.98	5.11	2.52	2.08	0.17	0.77	0.34	64.75	0.67	95.41

Sample code	Strat. Pos.	Ba ppm	Cr ppm	Ni ppm	Sr ppm	Zr ppm	As ppm	Ce ppm	Cu ppm	Ga ppm	Hf ppm	La ppm	Nb ppm	Nd ppm
σ^* (%)	-	0.16	0.12	0.34	0	0.06	0.02	0.13	0.03	0.03	1.54	0.22	0.01	0.09
B12	4	229	30	22	1105	42	0	16	9	2	4	9	1	12
B19	4.94	149	69	52	558	45	1	6	17	5	3	8	2	11
B24	5.745	194	9	18	2222	38	0	31	15	3	8	28	1	26
B30	8	124	15	21	1274	34	2	12	11	4	4	0	1	6
B42	11.4	176	274	26	1121	52	8	28	11	13	4	28	1	25
B59	20.46	283	49	35	1273	50	2	32	21	5	5	31	2	28
B88	22.71	73	0	12	1441	64	1	16	15	5	7	9	2	11
B92	22.91	376	42	36	1064	59	4	32	48	6	5	12	2	14
GC 5	31.28	580	33	32	1318	47	2	45	22	4	4	5	1	10
GC 9	35.28	180	24	32	1222	42	3	17	23	4	5	12	2	14
GC 16	42.36	332	40	33	1243	46	2	26	21	5	6	15	2	16
GC 22,45	48.45	270	21	28	1738	45	3	25	19	3	8	6	2	10
GC 26	52	401	17	24	1555	42	1	38	21	4	5	9	1	12
GC 26,55	52.55	382	30	29	1210	48	2	27	19	5	5	5	2	10
GC 27	53	321	28	24	854	36	1	17	19	4	3	9	2	12
GC 28	53.75	641	32	28	989	64	3	36	30	6	5	6	3	11
GC 32,5	58.37	785	31	30	1103	46	2	47	19	6	5	12	2	15
GC 37	63.02	297	32	45	1261	52	6	28	33	6	7	10	3	13
GC 39	65.03	266	39	37	1387	41	1	24	17	3	5	10	2	13
GC 42	68.03	426	50	29	1875	38	1	39	19	4	9	3	1	8
GC 43	69.03	383	32	25	1420	35	1	31	12	2	5	7	1	11
GC 49	75.03	94	0	14	1571	53	0	44	41	3	5	33	1	29
GC 51	77.03	574	39	34	1877	47	3	43	34	4	6	7	2	11
GC 61,5	87.53	168	51	42	1839	58	1	13	29	4	8	8	1	11
GC 64	90.03	165	17	26	1472	42	1	10	11	4	4	5	1	9
32,62	90.07	601	31	12	821	36	0	30	11	4	3	10	1	13
GC 66,5	92.53	387	24	32	1818	79	4	38	22	6	9	14	3	15
GC 67,5	93.53	255	27	36	1587	57	4	23	25	4	7	7	2	10
GC 70	96.03	553	21	28	1691	46	1	50	19	3	5	1	1	7
124,86	182.65	566	9	9	1084	58	0	36	32	5	6	8	3	11
174,15	232.29	370	75	38	266	67	3	22	29	7	3	16	2	18
199,75	257.54	1091	14	14	383	186	0	35	4	11	7	7	4	11
215,36	273.15	83	0	15	635	85	1	13	9	4	5	6	2	9
218,60	276.4	286	25	24	537	85	0	32	9	6	5	23	2	23
226,48	284.27	123	24	21	521	50	1	16	11	4	2	15	1	16
ISE921	-	566	124	44	205	301	40	82	102	15	9	42	16	37

Sample code	Strat. Pos.	Pb ppm	Pr ppm	Rb ppm	Rh ppm	S ppm	Sc ppm	Sn ppm	Th ppm	U ppm	V ppm	Y ppm	Zn ppm
σ* (%)	-	0.73	0.98	0.10	0.05	0.72	1.56	0.06	0.07	0.09	0.13	0.08	0.09
B12	4	1	3	11	35	188	7	2	2	4	60	19	42
B19	4.94	0	3	22	36	245	9	2	0	5	446	11	64
B24	5.745	2	7	6	27	163	9	0	3	16	47	43	49
B30	8	1	1	11	29	297	9	2	0	6	93	15	64
B42	11.4	0	7	61	27	382	13	1	9	2	173	48	108
B59	20.455	0	7	15	31	336	11	0	0	3	103	53	81
B88	22.71	2	3	17	24	89	11	0	17	0	47	18	56
B92	22.905	2	4	23	32	618	12	2	2	3	89	22	140
GC 5	31.28	2	3	15	31	431	12	2	0	1	81	12	90
GC 9	35.28	0	4	14	29	395	10	1	5	3	64	13	100
GC 16	42.36	3	4	19	33	360	11	0	1	3	101	25	81
GC 22,45	48.45	2	3	12	31	464	11	1	0	5	70	22	77
GC 26	52	1	3	14	31	332	10	1	0	0	54	16	91
GC 26,55	52.55	0	3	14	33	409	8	0	10	2	95	13	70
GC 27	53	3	3	16	40	310	7	0	0	4	71	11	81
GC 28	53.75	2	3	23	35	307	10	0	2	2	101	15	77
GC 32,5	58.37	2	4	20	34	437	9	0	4	5	89	18	80
GC 37	63.02	4	3	27	32	471	10	4	0	6	416	15	103
GC 39	65.03	2	3	15	32	422	9	0	7	2	89	22	70
GC 42	68.03	0	2	11	30	251	11	2	0	0	95	9	67
GC 43	69.03	0	3	10	31	260	10	0	0	0	73	8	63
GC 49	75.03	2	8	12	24	43	9	1	0	0	31	56	60
GC 51	77.03	0	3	11	32	511	10	0	0	4	70	19	108
GC 61,5	87.53	4	3	12	31	445	10	0	10	5	97	14	122
GC 64	90.03	2	2	10	29	265	9	0	10	2	64	9	57
32,62	90.07	0	3	10	37	238	7	1	0	3	51	16	35
GC 66,5	92.53	4	4	21	30	638	9	0	0	3	61	12	107
GC 67,5	93.53	2	3	18	30	770	9	1	1	2	64	16	86
GC 70	96.03	0	2	9	30	316	9	0	0	0	43	11	84
124,86	182.65	3	3	23	36	79	7	0	1	2	25	14	50
174,15	232.29	2	5	17	37	714	12	3	0	2	156	25	104
199,75	257.54	2	3	31	37	113	10	1	0	2	49	26	86
215,36	273.15	3	3	6	25	270	10	1	7	1	53	15	57
218,60	276.4	2	6	19	38	183	11	2	0	4	80	52	41
226,48	284.27	1	4	12	29	260	12	0	2	2	136	22	64
ISE921	-	197	10	124	28	84	14	15	14	3	98	31	618

*Precision of the machinery, expressed in standard deviation per element in percent.

Appendix E: Grain size data table

Code	Strat. Pos.	Obscuration %	d(0.10) μm	d(0.5) μm	d(0.90) μm	Mode μm	<20 μm	>20<63 μm	>63 μm
B30	8	21.44	0.876	2.01	6.763	1.855	98.7700	0.77966	0.45031
B75	21.40	19.72	0.875	3.047	295.961	146.191	58.5729	1.28537	40.1417
GC1	27.28	21.8	0.622	2.781	11.398	1.558	98.7467	1.25333	0
GC2	28.31	21.85	0.611	2.2	6.689	2.225	99.6342	0.36581	0
GC3	29.28	21.23	0.614	1.784	5.451	1.748	99.9790	0.02102	0
GC5	31.28	20.49	0.632	1.714	5.513	1.628	99.9771	0.02292	0
GC17	43.36	20.83	0.633	6.398	20.388	12.131	89.4675	10.5325	0
GC17 MD	43.36	20.65	0.658	6.396	20.323	12.138	89.5527	10.4473	0
GC26	52.00	21.9	0.675	1.93	6.502	1.704	100	0	0
GC29	54.98	20.29	0.616	2.2	11.692	1.919	93.4717	4.03834	2.48998
GC32	57.87	21.16	0.599	1.436	3.87	1.47	100	0	0
GC32.5	58.37	18.02	0.62	1.346	5.298	1.285	93.0766	0.64201	6.28138
GC33.5	59.37	21.17	0.665	1.338	3.09	1.441	99.9674	0.03262	0
GC33.5 OD	59.37	21.26	0.552	1.336	3.079	1.439	99.9678	0.0322	0
GC36.5	62.52	21.53	0.552	2.082	8.731	1.596	97.8369	0.73570	1.42738
GC37.5	63.52	21.34	0.574	1.487	4.048	1.525	99.9673	0.03271	0
GC38	64.02	19.7	0.805	1.504	4.027	1.561	98.5669	1.30607	0.12706
GC43	69.03	19.22	0.919	2.36	8.855	2.256	93.2672	0.67285	6.0600
GC46	71.91	21.22	0.548	1.957	8.879	1.538	95.1613	0.52089	4.31784
GC46 OD2	71.91	21.38	0.608	2.028	9.339	1.604	94.5462	0.65255	4.80127
GC50	75.51	20.22	0.56	2.668	6.678	2.872	100	0	0
GC51	77.03	21.14	0.697	2.179	8.789	1.587	99.7666	0.23344	0
GC52	78.03	21.4	0.704	1.307	2.962	1.41	100	0	0
GC63	89.03	20.91	0.553	2.023	7.069	1.716	100	0	0
GC64	90.03	21.59	0.531	1.765	8.427	1.63	93.3636	2.81300	3.82336
GC67.5	93.53	20.95	0.583	1.5	5.677	1.442	95.6626	1.98047	2.35696
GC69	95.36	21.73	0.652	2.412	9.9	2.075	94.5960	1.84382	3.56018
173.7	231.49	21.73	0.63	2.207	9.362	1.701	96.7303	1.14060	2.12912

MD = Machinery Duplicate, measuring the same subsample twice to check for bias produced by the machinery.

OD = Operator Duplicate, measuring two different subsamples of a sample to check for bias produced by the operator.